UNIVERSITÀ DEGLI STUDI DI PADOVA

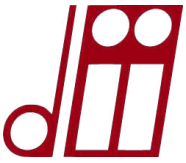

UNIVERSITÀ DEGLI STUDI DI PADOVA

Dipartimento di Ingegneria Industriale DII

Corso di Laurea Magistrale in Ingegneria dell'Energia Elettrica

Tesi di Laurea

Development of a Numerical Tool for the Optimization of the Injection Angle of Electron Cyclotron Wave in TCV

Relatore: Prof. Paolo Bettini

Supervisore: Dott. Mario Ludovico Podestà

Fabio Bortolazzi 2091012

Anno Accademico 2024/2025

Abstract

TCV (Tokamak à Configuration Variable) is the tokamak operated at the Swiss Plasma Center (SPC) in Lausanne. Thanks to its high versatility, it allows the study of plasmas under a wide range of different configurations, making it a key facility for international research on nuclear fusion. TCV is equipped with a high-power Electron Cyclotron Resonance Heating & Current Drive (ECRH-ECCD) system, which enables both plasma heating and non-inductive current drive through the injection of electron cyclotron (EC) waves. Many parameters influence the performance of this system, including the injected power, the wave frequency and the injection angle.

EC waves are launched into the plasma by means of antennas equipped with steerable mirrors, which can modify the injection direction during the operation. This thesis focuses on the optimization of the EC wave injection angle, a key parameter that can strongly affect the efficiency of the ECRH system.

Currently, the choice of the injection angle at TCV is mainly based on previous experience or on a try-and-error approach. The aim of the work carried out at the Swiss Plasma Center was to develop a numerical tool able to estimate the optimal antennas injection angles for a given scenario, by means of simulations performed using the TORAY ray tracing code. In particular, the optimization was applied to two different objectives: maximizing the fraction of power absorbed by the plasma and maximizing the radio frequency current drive. The practical purpose for this work was to offer to the ECRH operator in the TCV control room a tool capable of providing a first qualitative indication of the most suitable injection angles to adopt for a given experiment, based on the the chosen optimization criterion.

In order to validate the tool, experiments on TCV were carried out considering different plasma scenarios. These tests proved that the use of this newly developed tool could be beneficial, especially for plasmas with parameters that change over time. However, while the code provides reliable results in simple scenarios, more physically complex plasma configurations might require an adjustment of the calculated angles, to take into account variables which are not considered by TORAY.

The first two chapters of this thesis offer a general overview of nuclear fusion, tokamaks, plasma physics, and wave propagation in plasmas, as well as an introduction to the electron cyclotron resonance heating technique. Chapter 3 describes the main features of the TCV tokamak and its ECRH system, while Chapter 4 focuses on the description of the developed tool and the methodologies used to optimize the microwave injection angles, including a brief overview of the functioning of the codes already present at the Swiss Plasma Center, which have been used for this thesis. A preliminary analysis is presented in Chapter 5, in which a possible misalignment of the ECRH antennas inside the vessel was investigated and quantified. In Chapter 6, the validity of the developed tool is tested through a set of dedicated TCV experiments aimed at maximizing both power deposition and driven current. Finally, Chapter 7 provides a summary of the results and concluding remarks, also introducing possible future developments.

Table of Contents

Chapter 1

Introduction

1.1 Nuclear fusion

Nuclear fusion is a process that takes place naturally in stars. During the 20th century, scientists aimed to explain the origin of all chemical elements and their observed relative distribution in known matter. Although earlier theories assumed that elements were formed during the primordial stages of the universe, a new theory was developed in 1957 by Burbidge et al., proposing that elements originated inside the stars [1]. Stars are subjected to an enormous gravitational pressure, generated by their own mass; these extreme conditions enable nuclear reactions to occur in their cores. In particular, hydrogen atoms – the most abundant element in newborn stars – undergo fusion: two hydrogen nuclei fuse to form a heavier nucleus, such as helium. These newly formed elements can then undergo further fusion reactions, producing even heavier elements. This process, known as stellar nucleosythesis, explains the origin of all the known elements, which were generated either within stars or in subsequent cataclysmic events such as supernovae.

An enormous amount of energy is released during fusion reactions, and this is what sustains the high temperature of a star, preventing the star from collapsing on itself due to gravitational force.

The idea of replicating on Earth what naturally occurs in stars is not only a dream for the astrophysicists, but it is a concrete opportunity that could offer a potentially clean, safe and sustainable solution to the always increasing global demand of energy.

1.1.1 Nuclear fusion for energy production

The global energy demand grows year after year. According to the IEA Global Energy Review 2025, global energy consumption increased by 2.2% in 2024 compared to the previous year [2]. Electricity demand grew even more rapidly, increasing by 4.3%

in 2024, driven by growing trends such as electricity intensive appliances (e.g., air conditioning and manufacturing) as well as increasing power demand from digitization, data centers and AI and from the electrification of end uses. Overall, the power sector accounted for three-fifths of the total increase in global energy demand.

In response to this ever-growing electricity demand, all major energy systems experienced expansion in 2024. Although the biggest development was recorded for renewable technologies and other non-fossil fuel energy sources, also natural gas, oil and coal saw growth, highlighting how the world still heavily depends on fossil fuels for electricity production. This fact is evident in Figure 1.1, which shows the distribution of global electricity produced by source in 2022 [3]. Despite the recent large expansion of renewable sources, more than half of the total electricity was still generated using traditional fossil fuels. The use of fossil fuels for electricity production has important environ-

Figure 1.1: Global electricity generation by source in 2022. Source: [3].

mental consequences, including global warming, air pollution and ecological damage consequent to resource extraction. Moreover, fossil fuels are unevenly distributed on the planet and non-renewable, raising the problem of their availability for this and future generations [4].

With an constantly increasing demand for electricity and the urgent need to reduce dependence on fossil fuels, clean energy production is one of the greatest challenges of our time. The transition to clean energy systems is essential to ensure the high living standards of OECD member states while enabling sustainable development in emerging economies. Many countries around the world are making significant efforts to reduce the human impact on the environment by substituting the use of fossil fuels, including through the exploration of new alternative technologies for electricity production.

One of the most promising candidates for sustainable electricity generation is nuclear fusion. This technology involves nuclear reactions, like the already widely used nuclear fission, but the physical principle is completely different: instead of splitting a heavy radioactive nucleus to release energy, fusion combines two light nuclei together to form a heavier atom, emulating the same process that powers stars. The resulting nucleus has a lower mass than the sum of the original particles: the mass difference is released as energy [5].

Nuclear fusion offers several important advantages. First, it produces a very limited amount of waste, compared with other technologies. The product of the nuclear reaction is helium, which is not pollutant or radioactive, and the only radioactive waste, limited to the structure materials with neutron-induced activation, are not long-lived radioactive waste [6]. In addition, the fuel used for the reaction is a mixture of deuterium and tritium, which are substantially inexhaustible. The first is highly present in ocean water – 33 g of deuterium are present in 1 m^3 of water – while the second can be produced inside the reactor itself from lithium, which is also very abundant and widely distributed on Earth. Finally, fusion is intrinsically safe since any accident that disturbs the burning condition would cause the fusion reaction to stop spontaneously, unlike nuclear fission, where the chain reaction can run out of control in case of problems.

1.1.2 Physics of nuclear fusion reactions

A variety of fusion reactions can release energy when they occur. Each of them is characterized by a specific reaction probability, referred to as *cross section* σ [m^2] [6]. The primary fusion process occurring in the Sun is the proton–proton chain reaction [5], expressed as:

$$4\mathrm{p} \rightarrow \mathrm{He}^{++} + 2\mathrm{e}^{+} + 2\nu_e + 2\gamma \tag{1.1}$$

Through a series of steps, four protons fuse to form a nucleus of helium. However, this reaction has an extremely low cross section, as on average one proton fuses every billion years [5]. The Sun can still keep burning because of its immense dimension, but it is clear that the same reaction cannot be used on Earth for electricity generation. A fusion reaction involving hydrogen isotopes – deuterium (D) and tritium (T) – offers a much higher cross section and is considered the most suitable for terrestrial applications. The two isotopes are fused to produce one nucleus of helium (He) and one neutron (n) [6], as shown in Eq. 1.2:

$$\mathrm{D} + \mathrm{T} \rightarrow \mathrm{He} + \mathrm{n} \tag{1.2}$$

This reaction releases a total of 17.6 MeV as kinetic energy, with 3.5 MeV carried by the α-particle – the helium nucleus – and 14.1 MeV by the neutron. In order to induce the fusion of nuclei of deuterium and tritium, it is necessary to overcome the mutual electrostatic repulsion [7]. As a result, the cross section is strongly dependent on the kinetic energy of the colliding nuclei, as illustrated in Figure 1.2. The D-T fusion cross section shows a peak in correspondence of approximately 100 keV.

The most practical way to supply this energy is by heating the fuel to a sufficiently high temperature so that the thermal velocities of the nuclei are high enough to induce the reaction. In practice, the target temperature in fusion experiments is around 10

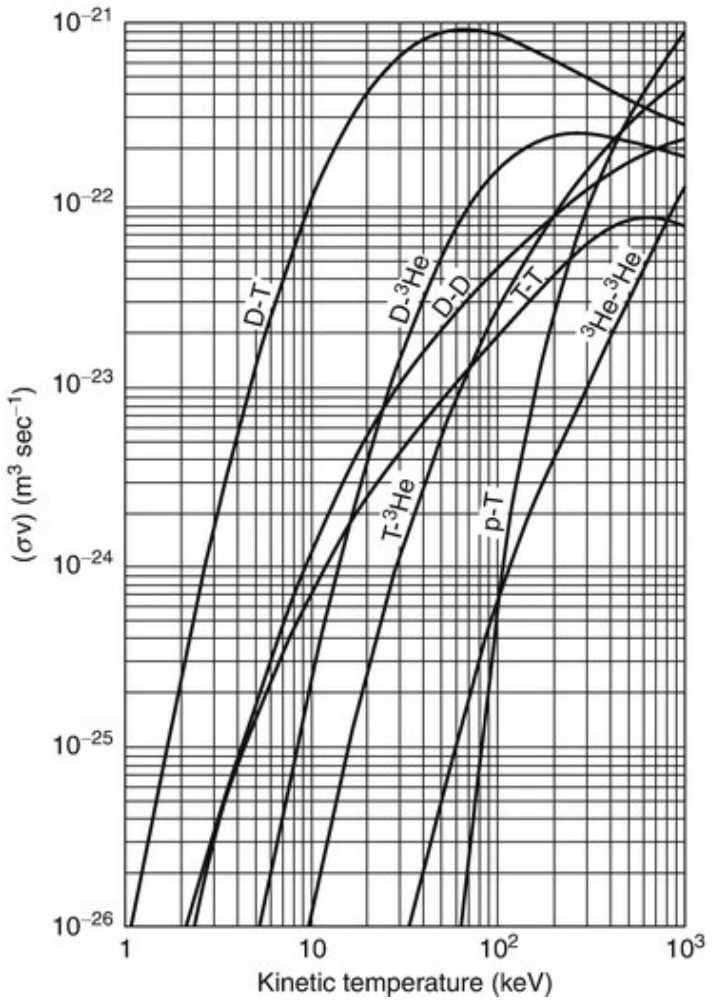

Figure 1.2: Cross section as a function of the kinetic energy of the colliding nuclei, for different possible nuclear fusion reaction. The D-T curve shows a peak at approximately 100 keV. Source: [5]

keV – about 100 million °C – which does not correspond to the peak of the cross section, but allows reactions to occur in the high-energy tail of the Maxwellian distribution of particle energies [7]. At such high temperatures, the fusion fuel becomes fully ionized, entering a state of matter known as plasma.

1.1.3 Magnetically confined nuclear fusion

Due to the extremely high temperatures required for fusion reactions to occur, the plasma cannot be confined by material walls. Therefore, an alternative confinement method is necessary. Two major approaches are currently being studied to achieve fusion energy: inertial confinement fusion and magnetic confinement fusion.

In inertial confinement nuclear fusion, a spherical fuel pellet is rapidly compressed by an intense pulse of radiation or energetic particles. This compression generates the conditions required for fusion reactions to take place, while the reacting fuel remains contained by its own inertia for a very short time. The process is repeated many times per second to produce fusion power.

In contrast, in the magnetic confinement fusion approach, the fuel is confined inside a particular toroidal structure, denoted as tokamak[1], by means of an intense toroidal magnetic field, which is generated by external superconducting magnets. This type of confinement exploits the fact that charged particles move helically around magnetic field lines, and in this way they are magnetically confined in the direction orthogonal to the toroidal field, while they are free to move along the field lines. However, a simple toroidal magnetic field alone cannot provide efficient confinement because of its radial gradient, consequent to the toroidal shape. This configuration indeed generates a magnetic field that is stronger near the axis of the tokamak and decreases with the radial distance; this gradient causes particles to drift outward, leading to poor confinement. To compensate for this, the magnetic field lines must be twisted by adding a poloidal component to the magnetic field. This additional component is generated by inducing a toroidal current in the plasma, treating the plasma as the secondary winding of a transformer [5]. The resulting helical magnetic field improves particle confinement by reducing radial drifts. Figure 1.3 illustrates the tokamak structure and the two magnetic field components. The high temperatures necessary for magnetically confined fusion are achieved through the ohmic heating provided by the induced plasma current and by additional external heating systems [9].

In this thesis, magnetic confinement nuclear fusion technology will be considered.

[1] The tokamak is the most widely studied magnetic confinement device, but other configurations, such as the stellarator and the heliotron, are also being explored [6].

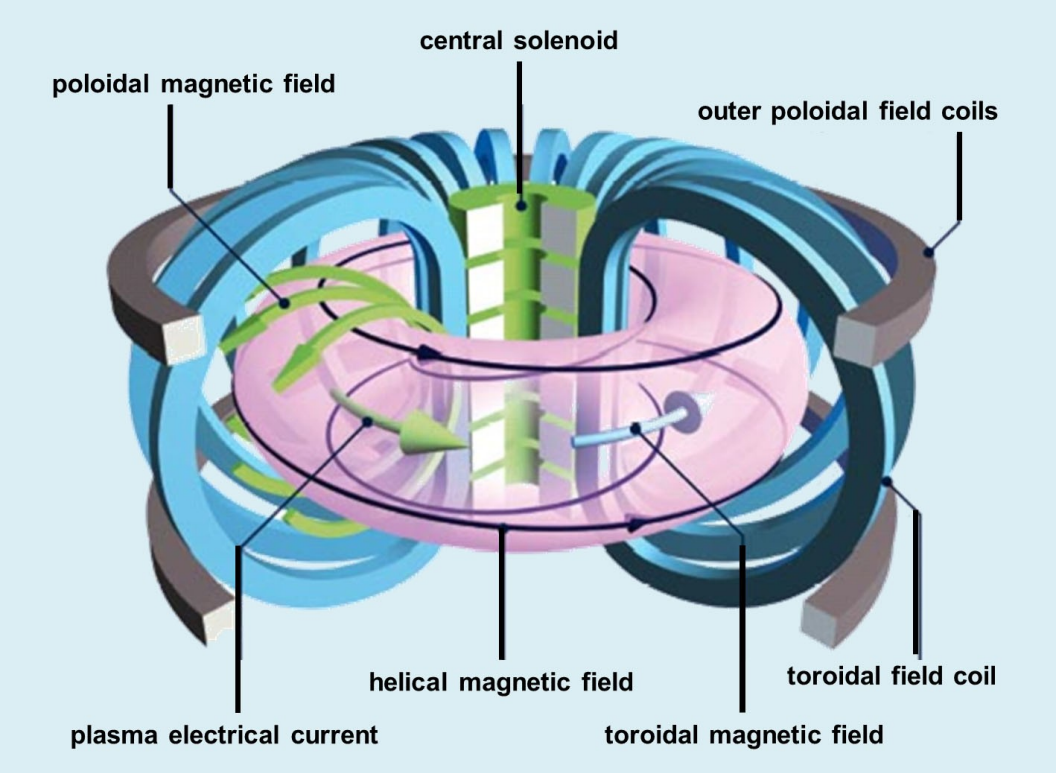

Figure 1.3: Tokamak structure with the different components of the magnetic field. The central solenoid induces a toroidal plasma current, which generates the poloidal component of the magnetic field and heats the plasma via ohmic effect. Source: [8].

Chapter 2

Plasma Heating and Current Drive

As introduced in Section 1.1.2, the D-T fusion reaction requires extremely high temperatures inside a fusion reactor to achieve a sufficiently large cross section. The primary heating mechanism in a tokamak is ohmic heating: a poloidal magnetic field component can be generated by inducing a toroidal current in the plasma, which is also useful for heating the plasma through ohmic effect. However, plasma resistivity decreases with temperature, approximately as $T_e^{-\frac{3}{2}}$, resulting in less effective ohmic heating at high temperatures. Furthermore, the maximum plasma current that can be sustained for a given toroidal magnetic field is limited by plasma instabilities, introducing a constraint on the maximum temperature achievable by ohmic heating to around 3 keV. A second heating source is provided by α-particles (helium nuclei), which thanks to the energy released by the fusion reaction can heat the plasma by colliding with other particles. However, this mechanism only becomes relevant at high temperatures, typically in the range of 5-7 keV [10]. Therefore, in order to reach higher temperatures, additional external heating systems are required.

There are two main methods for externally heating the plasma:

- injection of high energy neutral particles
- resonant absorption of radio-frequency (RF) electromagnetic waves

Both of these mechanisms are capable not only of heating the plasma, but also of driving a non-inductive current [10]. As explained in Section 1.1.2, the poloidal magnetic field required for confinement is normally generated by inducing a toroidal plasma current, treating the plasma as the secondary winding of a transformer. However, a constant toroidal electric field can only be sustained by a monotonically changing magnetic field, hence only temporarily, since the field is limited by the magnetic flux available in the primary circuit [11]. As a result, inductive current drive inherently limits tokamak operation to a pulsed regime. Pulsed functioning has many disadvantages compared to

steady-state operation, including thermal and mechanical stresses from cyclic heating, a higher frequency of plasma disruptions, and space constraints due to the central solenoid used for the transformer. To enable continuous operation, it is necessary to drive a constant toroidal current in the plasma. This can be achieved using the same external heating systems described above, both of which can contribute to non-inductive current drive.

The first system that can be employed for plasma heating and current drive is commonly known as NBI (neutral beam injection) and consists in the injection of high energy neutral particles into the plasma. These particles must be neutral in order to penetrate the magnetic field of the tokamak, which would otherwise deflect charged particles. Because it is easier to accelerate charged particles, the process begins by producing and accelerating ions to the required energy. These ions are then neutralized before being injected into the plasma. Once inside the plasma, the neutral atoms are re-ionized due to the high temperatures and become confined by the magnetic field. As they slow down through Coulomb collisions with plasma particles, they transfer energy to the bulk plasma, increasing the plasma temperature [7]. Moreover, if the beam is injected with a tangential component relative to the toroidal direction, NBI can contribute to the plasma current drive. As momentum is transferred from the beam to the plasma particles, their toroidal velocity increases – accordingly to the injection direction – resulting in a net non-inductive plasma current [10].

The second main external heating system is radio-frequency (RF) heating, which consists in the injection of radio-frequency electromagnetic waves into the plasma by means of antennas. Several types of RF heating exist, depending on the frequency range and the type of resonance that is exploited. The three principal mechanisms are [12]:

- ion cyclotron resonance heating (ICRH)
- electron cyclotron resonance heating (ECRH)
- lower hybrid resonance heating (LHRH)

All RF systems share a common architecture: a high-power RF generator, a transmission line to connect the generator to the tokamak and an antenna to couple the waves with the plasma. Once launched, RF waves must propagate through a non-uniform plasma and magnetic field. Their energy is then absorbed, typically in the plasma core, via collisionless mechanisms such as resonant wave–particle interactions [7].

Electron Cyclotron Resonance Heating (ECRH) is described in detail in Section 2.1, as it represents the main focus of this thesis.

2.1 Electron cyclotron resonance heating (ECRH)

Electron cyclotron resonance heating uses electromagnetic radiation at the electron cyclotron frequency – or its harmonics – to heat the plasma. Typical frequencies are of the order of a few gigahertz, corresponding to wavelengths of a few millimeters [13]. One advantage of this type of RF heating, compared to the other methods, is that the high frequency allows for less problematic coupling with the plasma, enabling the installation of antennas farther from the plasma edge, reducing the risk of arcing and unwanted plasma breakdown [10].

Electron cyclotron waves are generated by a device called *gyrotron*, which converts electrical power into electromagnetic radiation. This radiation is then transmitted via low losses waveguides to the tokamak, where the coupling with the plasma is assured by antennas. Inside the plasma, the power is carried by plasma waves – typically the extraordinary mode (X mode) is used – and is absorbed by the electrons through wave-particle interactions at the electron cyclotron frequency or its harmonics.

2.1.1 Gyrotron

A gyrotron is a millimeter wave source capable of delivering electromagnetic power on the order of megawatts. Its main components are an electron gun, a resonant cavity, a mode converter, a collector and an exit window. The electron gun generates an annular beam of electrons, which are accelerated by an electric field inside a vacuum tube. The gun also serves as the anode of the electrodes producing the electric field. The electrons follow a helical trajectory around magnetic field lines generated by external superconducting magnets. This rotational motion occurs at the electron cyclotron frequency, given by Eqn. 2.1. The Lorenz factor γ in the equation appears because the electrons reach relativistic velocities, and thus the mass must be corrected by using the relativistic mass, given by Eqn. 2.2.

$$\omega_{ce} = \frac{eB}{\gamma m} \tag{2.1}$$

$$m_r = \gamma m \tag{2.2}$$

As the electron beam reaches the resonant cavity – where the magnetic field is the strongest – the electrons interact with a specific transverse electric (TE) mode. Assuming a random initial phase between the electrons and the wave, some electrons are accelerated while others are decelerated. When an electron is decelerated, it loses energy, its relativistic mass decreases, and its cyclotron frequency increases. According to Eqn. 2.1, this leads to a phase shift that reduces further deceleration. Conversely, for an accelerated electron, the phase shift limits further acceleration. As a result,

phase bunching occurs: electrons tend to align in phase, leading to a net deceleration of the beam and the emission of coherent electromagnetic radiation perpendicular to the axis of the device. This is how microwave power is generated from the beam's perpendicular kinetic energy, with conversion efficiencies of up to 75%. The generated radiation can be converted into another filed profile (mode) thanks to the mode converter, before being directed via several mirrors to the exit window, where it exits the gyrotron. The electron beam with the residual energy is directed against the collector, where the remaining power is dissipated as heat [13], [14], [15]. Figure 2.1 shows a schematic of a gyrotron, highlighting the components described above.

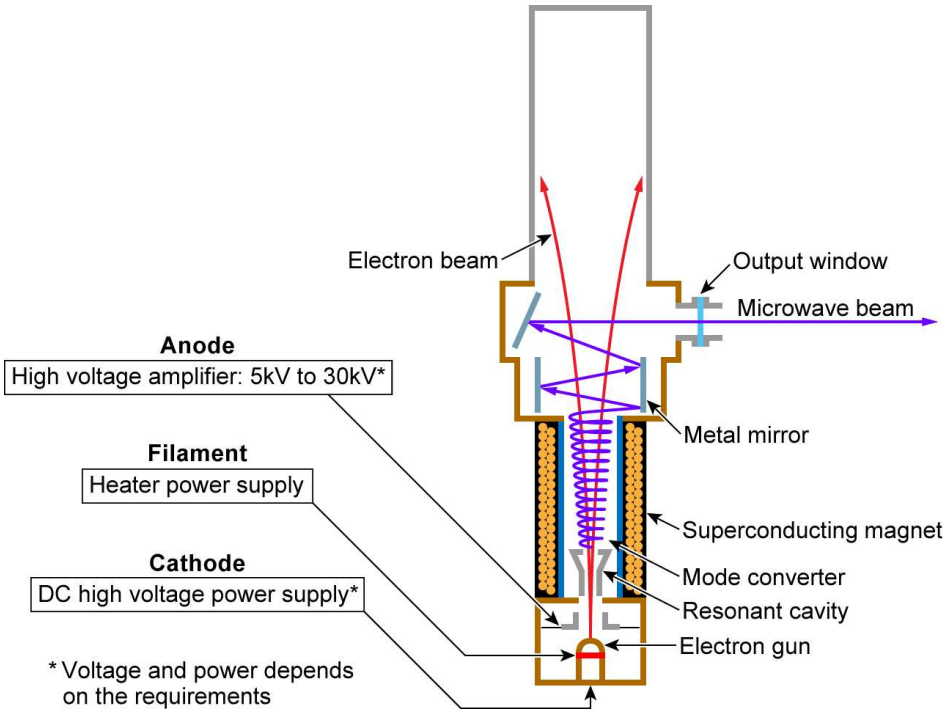

Figure 2.1: Schematic of a gyrotron structure. Source: [16].

Gyrotrons are typically optimized to operate at a single frequency; however, multi-frequency gyrotrons have recently been developed.

2.1.2 Transmission and launching of EC waves

Radio-frequency waves generated by the gyrotron are transmitted to the tokamak by either waveguides or quasi-optical systems. A critical component in this transmission line is the gyrotron output window, which must separate the high vacuum inside the gyrotron from the conditions inside the waveguide while transmitting high-power without significant losses. This is typically achieved using diamond windows, due to their excellent thermal conductivity and low dielectric losses [13]. A more detailed description of the specific waveguide system for TCV is provided in Section 3.1.3.

The EC waves are then injected in correspondence with the plasma edge by means of an antenna, which can be equipped with directional mirrors in order to modify in real-time the injection direction.

2.1.3 Propagation and absorption of EC waves

Due to the toroidal shape, the magnetic field inside of the tokamak is not spatially uniform, but it is a function of the tokamak's major radius. Specifically, the magnetic field reaches a maximum on the inner region (closer to the central axis) and decreases moving in radial direction. The inner side of the tokamak, where the magnetic field is strongest, is referred to as *high-field side* (HFS), while the outer one is known as *low-field side* (LFS). Given the relationship between the electron cyclotron frequency ω_c and the magnetic field B (see Eqn. 2.1), the radial dependency of B also leads to a radial variation of ω_c, which increases moving closer to the axis of the tokamak [7], [13].

Absorption of EC waves occurs when the cyclotron frequency ω of the injected EC wave is the same as the electron cyclotron frequency of the plasma electrons ω_c: under this resonance condition, energy is transferred from the wave to the electrons. This is the fundamental mechanism behind electron cyclotron resonance heating. Due to the dependence of the electron cyclotron frequency on the radius, the resonance condition $\omega_c = \omega$ is satisfied only in a narrow region of the plasma. This region is referred to as the electron cyclotron resonance (ECR) layer and is represented as a straight vertical line in the subfigures of Figure 2.4. Thus, by choosing the wave frequency, it is possible to deposit power at a specific radial position in the plasma. The width of the ECR layer arises from the frequency shift by the Doppler effect and relativistic mass effects, and is typically about 1 cm wide, influenced by electron temperature, direction of the wave and intensity of the magnetic field [17].

Therefore, cyclotron waves injected from the antennas must propagate inside the plasma to reach the ECR layer and be absorbed. The propagation of a wave within a medium is described by the *dispersion relation* (Eqn. 2.3), which links the wave frequency ω with its propagation constant $\vec{k}$ (representing the number of wavelengths contained in 2π meters) [18].

$$\omega = \omega(\vec{k}) \tag{2.3}$$

Two important quantities defined based on ω and $\vec{k}$ are the phase velocity v_ϕ and the group velocity v_g, defined as:

$$v_\phi = \frac{\omega}{k} \tag{2.4}$$

$$v_g = \frac{\partial \omega}{\partial k} \tag{2.5}$$

The phase velocity represents the speed at which individual wavefronts (or the phase of the wave) travel, while the group velocity indicates the speed at which the wave energy is transported.

The dispersion relation for electromagnetic waves in plasma can be derived from Maxwell's equations together with the equation of motion for the electrons [12], and is fundamental for understanding whether a wave can propagate through the plasma or is reflected, depending on local plasma conditions. Two particularly important behaviors occur when the wave number k approaches zero or infinity; these conditions are called *cut-off* and *resonance*, respectively. The complex refractive index $\tilde{N}$ is defined as:

$$\tilde{N} = \frac{c}{v_\phi} = \frac{ck}{\omega} \tag{2.6}$$

From this, it follows that:

- in the cut-off condition $k \to 0$, so the refractive index $\tilde{N} \to 0$
- in the resonance condition $k \to \infty$, so $\tilde{N} \to \infty$

As a wave propagates through a region where plasma parameters – such as magnetic field or plasma density – vary, it may encounter cut-offs and resonances. A wave is generally reflected at a cut-off and absorbed at a resonance.

Two kinds of electromagnetic waves can be used to propagate the power inside the plasma: the *extraordinary mode* (X-mode) and the *ordinary mode* (O-mode). These modes differ in the polarization of the wave's electric field relative to the background magnetic field $\vec{B_0}$. Assuming wave propagation is perpendicular to the magnetic field ($\vec{k} \perp \vec{B_0}$), and considering that for transverse waves the electric field is also perpendicular to the wave vector ($\vec{k} \perp \vec{E_1}$) [1], two distinct polarizations are possible: either $\vec{E_1} \parallel \vec{B_0}$ or $\vec{E_1} \perp \vec{B_0}$ [12].

Ordinary waves

In ordinary waves, the electric field is parallel to the magnetic field: $\vec{E_1} \parallel \vec{B_0}$. Figure 2.2a illustrates the injection of an ordinary wave into a plasma column, similar to what occurs in a tokamak.

The dispersion relation for O-mode waves is given by Eqn. 2.7 [12], where ω is the frequency of the wave, c is the speed of light and ω_p is the electron plasma frequency, defined by Eqn. 2.8.

$$\omega^2 = \omega_p^2 + c^2 k^2 \tag{2.7}$$

[1] The subscript "1" in E_1 indicates that only the fundamental harmonic of the oscillating electric field is considered, in order to have sinusoidal quantities.

$$\omega_p = \sqrt{\frac{e^2 n_e}{\epsilon_0 m_e}} \tag{2.8}$$

From Eqn. 2.7 it can be seen that when $\omega = \omega_p$, k becomes zero, and so does the refractive index, indicating that there is a cut-off condition.

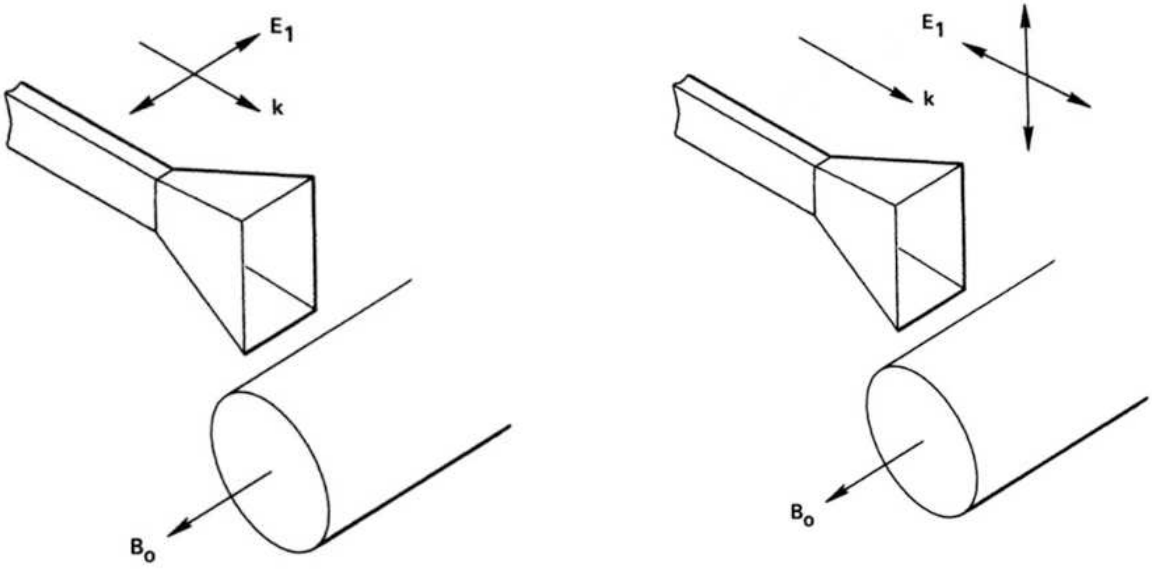

(a) Orientation of the electric field for an O-mode wave.

(b) Orientation of the electric field for an X-mode wave.

Figure 2.2: Waves launched from a waveguide antenna toward a magnetized plasma column. Source: [12].

Extraordinary waves

In extraordinary waves, the electric field is perpendicular to the magnetic field: $\vec{E_1} \perp \vec{B_0}$. Unlike O-mode waves, X-mode waves tend to be elliptically polarized rather than plane polarized. As they propagate through a plasma, they acquire a component of the electric field along $\vec{k}$, becoming partially longitudinal and partially transverse, in contrast to the fully transverse nature of O-mode waves [12]. The orientation of the fields involved in X-mode propagation is shown in Figure 6.1b.

The dispersion relation for extraordinary waves [12], [19] is given by :

$$N^2 = \frac{c^2 k^2}{\omega^2} = 1 - \frac{\omega_p^2}{\omega^2} \frac{\omega^2 - \omega_p^2}{\omega^2 - \omega_h^2} \tag{2.9}$$

where ω_h is the *upper hybrid frequency*, defined as:

$$\omega_h^2 = \omega_p^2 + \omega_c^2 \tag{2.10}$$

and ω_c is the electron cyclotron frequency:

$$\omega_c = \frac{eB}{m_e} \tag{2.11}$$

Cut-off conditions for extraordinary waves can be found by setting $k = 0$ in Eqn. 2.9 [12]. Two distinct cut-off frequencies are encountered:

$$\omega_R = \frac{1}{2}\omega_c + \frac{1}{2}\sqrt{\omega_c^2 + 4\omega_p^2} \tag{2.12}$$

$$\omega_L = -\frac{1}{2}\omega_c + \frac{1}{2}\sqrt{\omega_c^2 + 4\omega_p^2} \tag{2.13}$$

These are known respectively as *right-hand* (ω_R) and *left-hand* (ω_L) cut-off frequencies.

The resonance condition can be found by taking the limit $k \to \infty$ in the dispersion relation (Eqn. 2.9), which leads to a divergence in the refractive index. This occurs when $\omega = \omega_h$, corresponding to the upper hybrid resonance.

In summary, O waves have a single cut-off at $\omega = \omega_p$ and no resonances, while X-waves have two cut-off frequencies, ω_R and ω_L, and one resonance at $\omega = \omega_h$. Figure 2.3 shows the dispersion diagram for both wave modes, indicating their respective cut-offs and resonances. It can be seen that these frequencies divide the diagram into propagation and non-propagation regions.

In a tokamak the magnetic field B_0 is approximately inversely proportional to the major radius, $B \propto 1/R$, while the density n_e typically increases monotonically from the plasma edge toward the magnetic axis. This leads to a picture of the wave cut-offs and resonances inside the plasma as shown in Figure 2.4, given the dependency of the cut-off and resonance frequency on B_0 and n_e [19]. For the X-mode at the fundamental harmonic ($\omega = \omega_c$), two no-propagation areas – named evanescent layers – are present. In particular, the region between the right-hand cut-off (ω_R) and the upper hybrid resonance (ω_h) shields the fundamental resonance (ω_c) from waves injected from the LFS, which would be reflected. As a result, RF heating at the fundamental harmonic is only possible from the HFS. However, HFS launch is generally avoided due to technical challenges, including limited available space and increased attenuation along the waveguide path [17]. In order to access the ECR layer from the LFS, higher harmonics of the electron cyclotron frequency – such as the second or third harmonic – should be used; in this case the correspondent curve on the dispersion diagram of Figure 2.3b is referred to as "fast X mode", which is characterized by only one cut-off at $\omega = \omega_R$. Fundamental O-mode waves do not experience this kind of shielding, having a behavior similar to that of second harmonic X-mode waves, as shown in Figure 2.4. The ECR layer can be reached from either side of the plasma, as long as the resonance itself does not lie within the evanescence region.

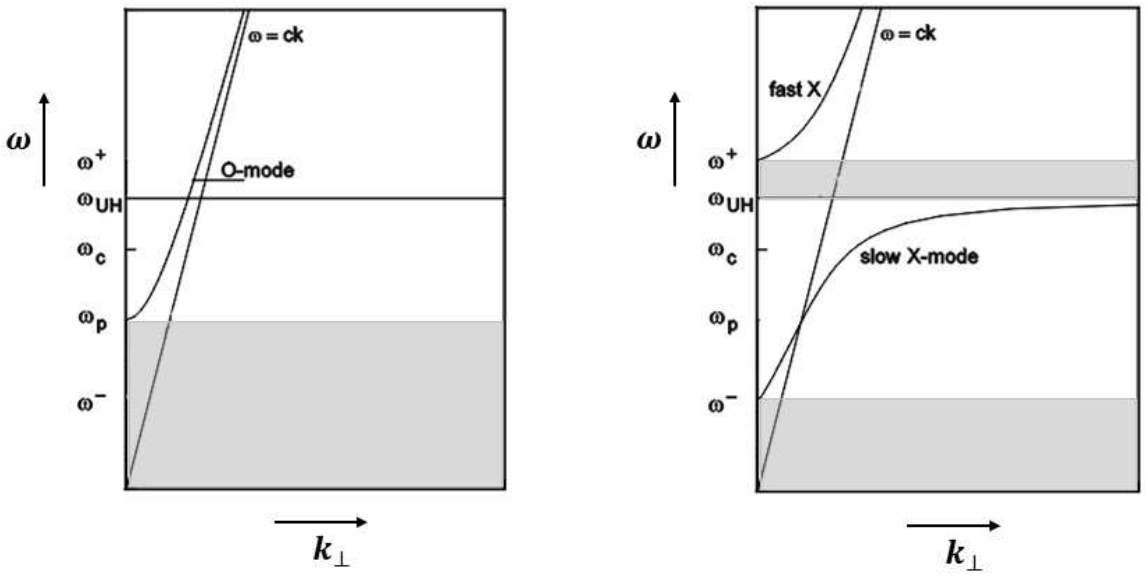

(a) Dispersion diagram for O-waves.

(b) Dispersion diagram for X-waves.

Figure 2.3: Dispersion diagram for O-mode and X-mode waves, showing cut-off and resonance frequencies. Right-hand cut-off frequency ω_R and left-hand cut-off frequency ω_L are indicated in the figure as ω^+ and ω^-, respectively. Regions of wave propagation and evanescence (shaded regions) are clearly identified. Source: [19], modified.

While electron cyclotron resonance is the primary mechanism for depositing RF power into the plasma, an alternative mechanism is also possible. As discussed, X-waves exhibit a resonance at the upper hybrid frequency ω_h. When the x-wave reaches the corresponding layer, it can undergo mode conversion into an electron Bernstein wave (EBW), which is not subject to electromagnetic cut-offs and can propagate deeper into the plasma. It is then absorbed at the first electron cyclotron resonance it encounters [7], [20].

2.2 Electron cyclotron current drive (ECCD)

The idea behind non-inductive current drive is to transfer energy to the electrons by injecting power via NBI or RF waves. In order to generate a net current inside the plasma, a toroidal asymmetry must be introduced: electrons moving in one toroidal direction must be accelerated more than those moving in the opposite direction, otherwise their contributions to the current would cancel out. Several methods exist to introduce an asymmetry, such as tangential NBI or tangential injection of waves, mainly Alfvén waves or lower hybrid waves, which can transfer net parallel momentum to slow (thermal) and fast (superthermal) electrons, respectively [11].

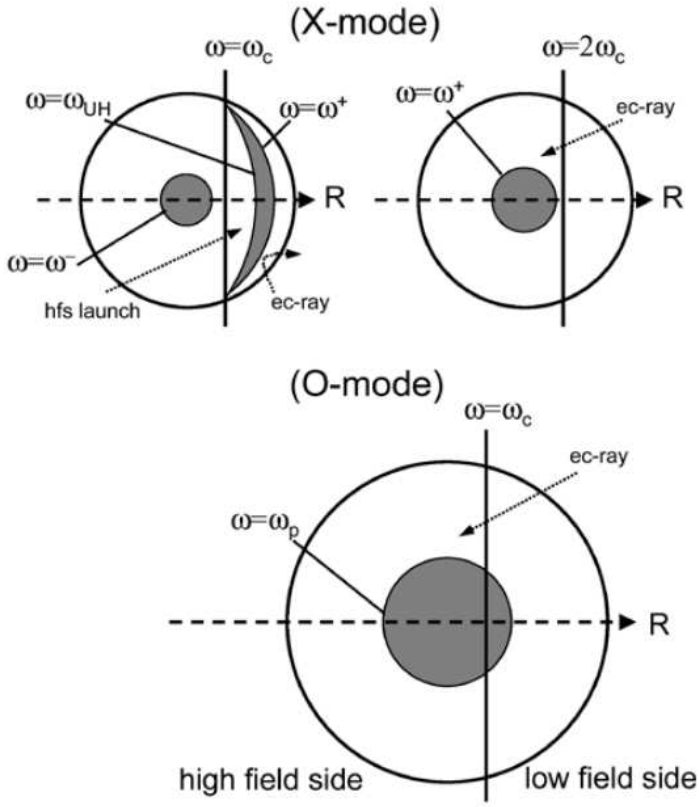

Figure 2.4: Wave cut-off and resonances in a poloidal cross section of a tokamak plasma. The upper figures show X-mode waves cases with either the fundamental or second harmonic resonance. The lower figure shows the case of the fundamental O-mode. Grey regions are the evanescent layers. Source: [19]

The electron velocity can be decomposed into two components, one parallel to the magnetic field, $v_\parallel$, and one perpendicular, $v_\perp$. The mechanisms mentioned above rely on an external source of parallel momentum. EC waves, in contrast, carry very little parallel momentum due to their predominantly perpendicular electric field, and therefore they primarily transfer energy to the $v_\perp$ component when the cyclotron resonance condition is satisfied. Nevertheless, EC waves can still drive current via a different, indirect mechanism. An electron moving in the toroidal direction generates a current, and the probability that the current is retained decays with time, because of collisions with other particles. It follows that this decay is quicker for slower, more collisional electrons. Figure 2.5 shows the current generated over time by two electrons with the same parallel velocity $v_\parallel$, but different perpendicular velocity $v_\perp$. Due to the dependence of the collision frequency on the electron velocity, an electron with higher $v_\perp$ can sustain the current for a longer time. Thus, if electrons moving in a specific toroidal direction are selectively accelerated perpendicularly by EC waves, those electrons will become more energetic and less collisional, introducing an asymmetry in the electron distribution function. This asymmetry can result in a net toroidal current. This preferential heating is achieved by obliquely launching the EC waves, with a tangential component of the wave vector: due to the Doppler shift, the resonance condition given by Eqn. 2.14 selects only electrons with a specific $v_\parallel$.

$$\omega - k_\parallel v_\parallel = \omega_c \tag{2.14}$$

By carefully choosing the injection angle, EC waves can therefore interact primarily with electrons moving in one toroidal direction, leading to electron cyclotron current drive [11].

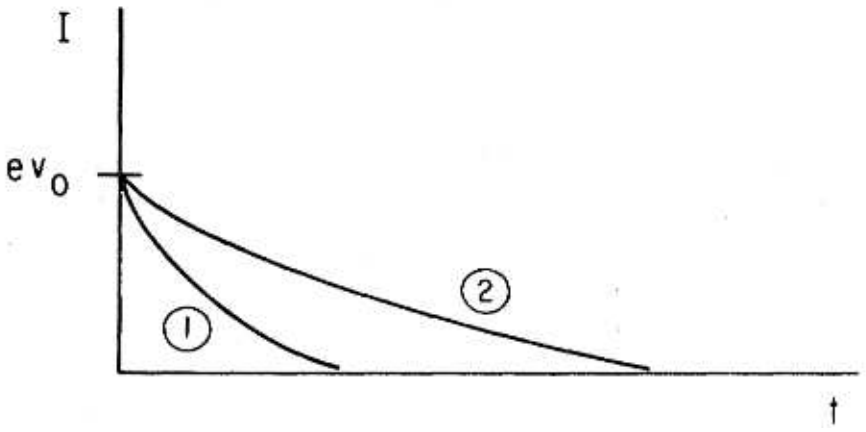

Figure 2.5: Current carried by two electron as a function of time, with $v_{2\perp} > v_{1\perp}$. The current carried by electron 2 is sustained for a longer time, due to its lower collision frequency. Source: [11].

Chapter 3

TCV tokamak

To provide a clearer understanding of the work carried out at the TCV facility, this chapter presents a general overview of the TCV tokamak, its plasma heating systems, and its operational procedures.

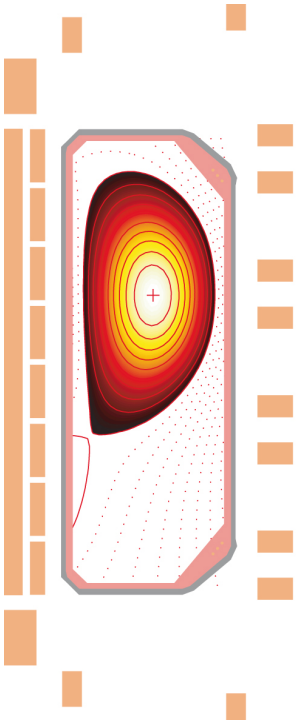

Figure 3.1: TCV vacuum vessel and poloidal coils. Source: [21].

TCV (Tokamak à Configuration Variable) is a medium-sized tokamak (major radius: R_0=0.88 m, minor radius: a=0.25 m) [22] with variable configuration, which, thanks to its specialized plasma shaping capability and a very high-power density ECRH & ECCD system, can produce several plasma configurations and plasma shapes without requiring hardware modifications. This flexibility allows to study how changes

in plasma configuration affect its properties, such as temperature and confinement quality [23].

TCV can work with a magnetic field up to 1.54 T, generated by 16 toroidal field coils. In addition to the toroidal field ones, other 16 poloidal field coils are used for plasma shaping; they are evenly distributed into two stacks located on both sides of the vacuum vessel, visible in Figure 3.1. In the same image also the 7 "OH-coils" are shown (the long rectangle and the three rectangles above and below the vessel). They are responsible for the inductive drive of the current into the plasma [21], which provides the poloidal component of the magnetic field, essential for plasma confinement, and ohmic heating. The plasma current can reach values of up to 1 MA.

In addition to ohmic heating, an auxiliary heating system is required in order to maintain the temperature high enough to allow nuclear reactions to take place. In TCV, the auxiliary heating is provided by a Neutral Beam Injection (NBI) system and an Electron Cyclotron Resonance Heating & Current Drive (ECRH-ECCD) system. Both systems also have a role in driving a non-inductive current in the plasma.

3.1 ECRH-ECCD system

The TCV ECRH-ECCD system is composed of six gyrotrons arranged into three clusters, each powered by a dedicated regulated high-voltage supply. The microwave beams produced by the gyrotrons are channeled, by means of the matching optics units, into waveguides that transmit the power to the antennas. These antennas, referred to as "launchers", finally inject the beam into the plasma, with the possibility of varying the injection angle.

Figure 3.2, illustrates the transmission line for a single gyrotron, from the source to the vessel. In the following paragraphs, a brief description of the main subsystems is given.

3.1.1 Gyrotrons

TCV is equipped with six gyrotrons capable of generating microwave beams at two different frequencies. All gyrotrons can operate at the second harmonic of the electron cyclotron frequency, while two of them can also generate waves at the third harmonic. This enables power deposition into plasmas with higher density, as the cutoff density for third harmonic waves is higher than that of the second harmonic [14]. The waves produced by the two types of gyrotrons from now on will be referred to as X2 and X3, where the "X" stands for "extraordinary wave", the X-mode being the most used.

For each gyrotron, the maximum pulse length is two seconds. Their characteristics are listed in the following [24]:

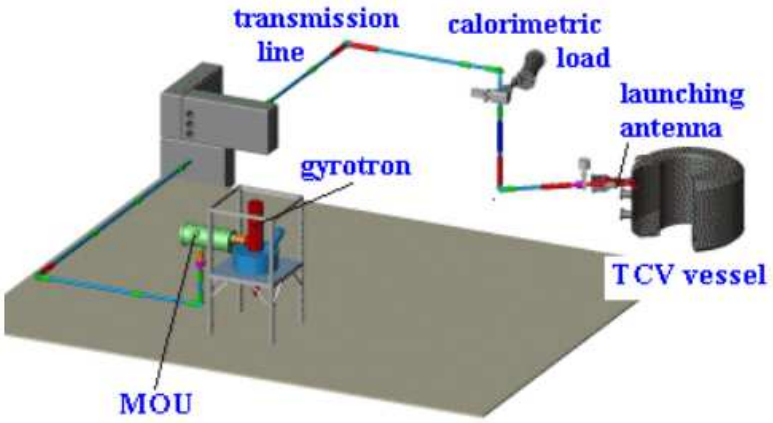

Figure 3.2: Transmission line for a single gyrotron. Source: [14].

- two 82.7 GHz gyrotrons (G1[1], G2) with nominal power of 750 kW, for heating at the second harmonic of electron cyclotron resonance
- two 118 Ghz gyrotrons (G7, G9) with nominal power of 500 kW, for heating at the third harmonic
- two double frequency gyrotrons (G10, G11) with nominal power of 1 MW, for heating either at second harmonic (84 GHz) or at third harmonic (126 GHz)

At the moment only gyrotrons G1, G10 and G11 are active, and it is planned to add another double-frequency gyrotron during 2025 [24].

3.1.2 Matching optics units

Each gyrotron is connected to a Matching Optics Unit (MOU) , which is located directly at the gyrotron window. The MOUs are needed to condition the microwave beam for good coupling with the transmission lines and the plasma. They are designed differently for X2 and X3 gyrotrons, due to the differences in the output beams.

The first function of a MOU is the coupling of the beam with the waveguide, which is achieved thanks to phase-correcting mirrors. Each MOU is also provided with grating polarizers that can change the beam polarization (linear to circular) [14]. In this way, it is possible to create extraordinary X-waves or ordinary O-waves. Since the

[1] From now on it will be used the nomenclature "Gx" to indicate a specific gyrotron, where the "x" stands for the number of the gyrotron. In a similar way the launchers will be referred to as "Lx".

second harmonic X-mode is absorbed better than second harmonic O-mode [13], the polarization of all beams is usually set to X-mode. In addition, MOUs can also provide beam filtering, absorbing undesired modes coming from the gyrotrons.

3.1.3 Transmission lines

The transmission lines connect the gyrotrons to the antennas, allowing the beams to reach the vessel. They consist of evacuated, corrugated waveguides made of aluminum alloy with an internal diameter of 63.5 mm. A typical waveguide run is ~30 m, with a transmission efficiency of ~96% [14]. The lines also include a high-power microwave switch to allow the beam to be diverted from the TCV direction to a calorimetric load. The beams are directed to the calorimetric loads to test the gyrotrons and during shots in which not all gyrotrons in the same cluster are used. The waveguides are also provided with fiber optic arc detectors, installed at the miter bends [25]. Both ends of each line are insulated using in-line DC breaks. Figure 3.3 shows a scheme of this configuration.

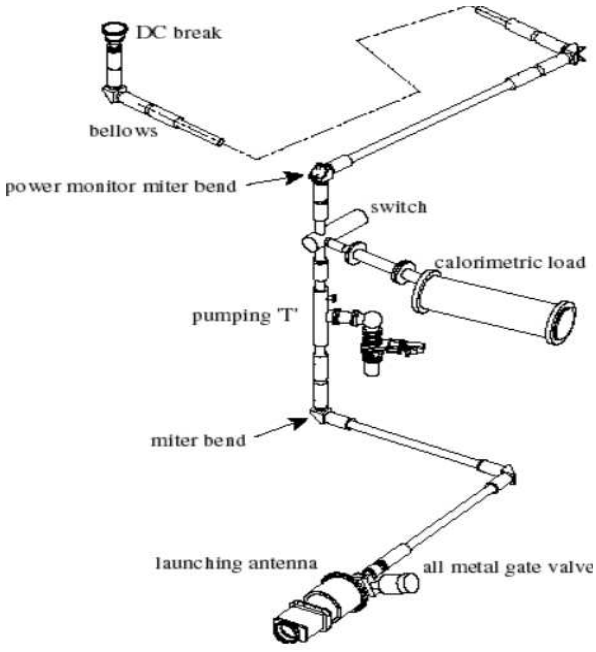

Figure 3.3: Configuration of transmission lines for TCV. Source: [14].

3.1.4 Launchers

The waves generated by the gyrotrons are injected into the plasma by means of six independent launchers. There is one launcher per transmission line. The possible gyrotron/launcher configurations and the position of the launchers in the poloidal plane

of the tokamak are shown in Figure 3.4, where it can be seen that the double frequency gyrotrons (G10 and G11) can inject waves from two launchers each, allowing power deposition from a lateral or from a top position. A more detailed scheme of the ECRH system is shown in Figure 3.5.

Gyrotron/Launcher	L1	L2	L4	L5	L10	L11
G1(82.7GHz/750kW)	X					
G2(82.7GHz/750kW)		X				
G7(118GHz/500kW)				X		
G9(118GHz/500kW)			X			
G10(84GHz/900kW)				X	X	
G10(126GHz/1000kW)				X	X	
G11(84GHz/900kW)			X			X
G11(126GHz/1000kW)			X			X

(a) Gyrotron/launcher possible configurations.

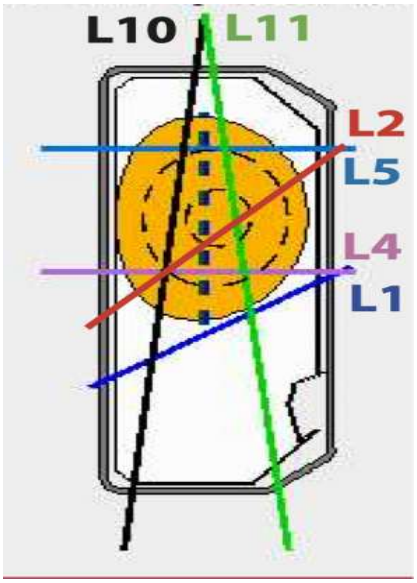

(b) Launchers positions on the vacuum chamber's cross section.

Figure 3.4: Configuration of the TCV ECRH-ECCD system. Source: [24].

Each launcher is equipped with mirrors that can be rotated, allowing to change the injection angle of the microwave beams. Beams passing through an equatorial launcher (L1, L4) or upper lateral launcher (L2, L5) have two degrees of freedom. The direction of the beam is defined by a couple of angles, which refers to the orientation of the last mirror interacting with the beam. Figure 3.6 shows an example of an X2 launcher, where the last mirror is labeled "M4". Considering the launcher pointing in the direction of the major radius of the tokamak and toward its center, and indicating this direction as the z-axis, a standard spherical coordinate system is used as a reference for the angles, as illustrated in Figure 3.7a. In this system, the *poloidal angle* of the launcher corresponds to the conventional θ, and the *toroidal angle* of the launcher corresponds to the conventional ϕ. The poloidal plane of the launcher is thus the cross-sectional plane shown in Figure 3.1, while the toroidal plane is tangent to the tokamak and orthogonal to the floor. From now on the direction of microwave injection for the equatorial (L1, L4) and upper lateral (L2, L5) launchers will be indicated referring to the coordinate system of Figure 3.7a, indicating the two angles interchangeably as poloidal and toroidal angles or as θ and ϕ.

The poloidal angle can be changed during a discharge at a speed up to 0.1°/ms,

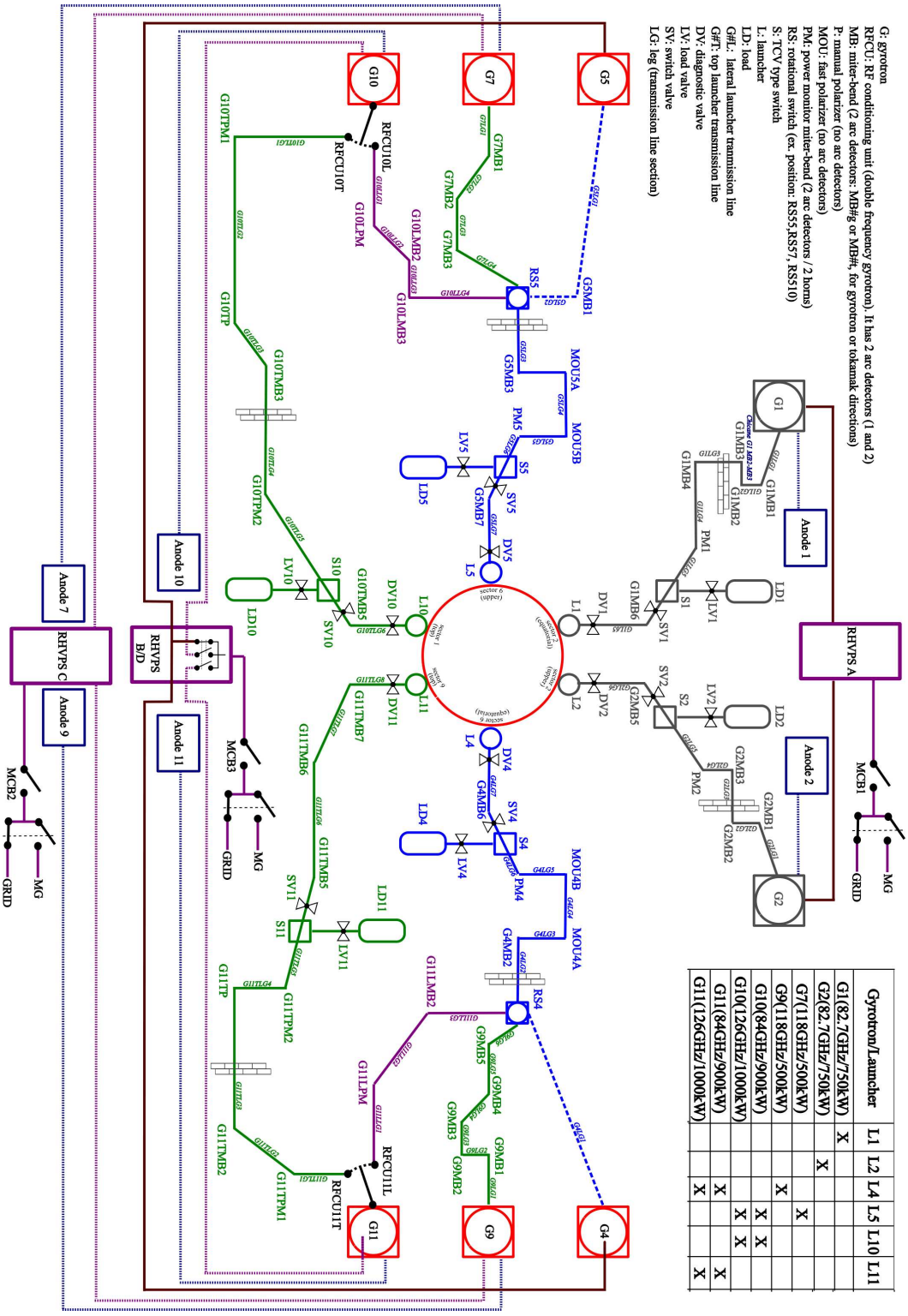

Gyrotron/Launcher	L1	L2	L4	L5	L10	L11
G1(82.7GHz/750kW)	X					
G2(82.7GHz/750kW)		X				
G7(118GHz/500kW)			X			
G9(118GHz/500kW)				X		
G10(84GHz/900kW)				X	X	
G10(126GHz/1000kW)				X	X	
G11(84GHz/900kW)			X			X
G11(126GHz/1000kW)			X			X

Figure 3.5: Scheme of TCV ECRH-ECCD system. Source: [24].

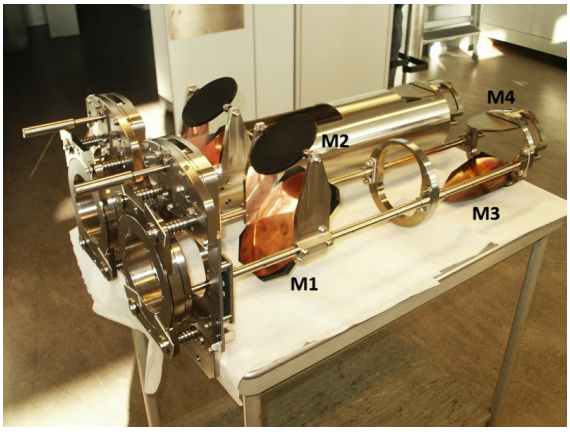

Figure 3.6: X2 launcher. Source: [22].

allowing for the deposition of power in different directions during the operation, while the toroidal angle can be modified only between discharges, for example to change the fraction of current driven by ECCD in the plasma.

Launchers in the upper port (L10, L11) provide the injected beams a direction that is almost perpendicular to the toroidal plane of the tokamak, increasing the path in the region of the plasma where the microwaves hit the electron cyclotron resonance (represented in Figure 3.4b with a dashed vertical line) and consequently improving power absorption. They have the same freedom of movement on the poloidal plane as the other launchers, while the toroidal angle ϕ is fixed. The reference system for the injection angles of L10 and L11 is shown in Figure 3.7b. Adopting this coordinate system, the toroidal angle for L10 and L11 is fixed, respectively, to -2.92° and -2.59°.

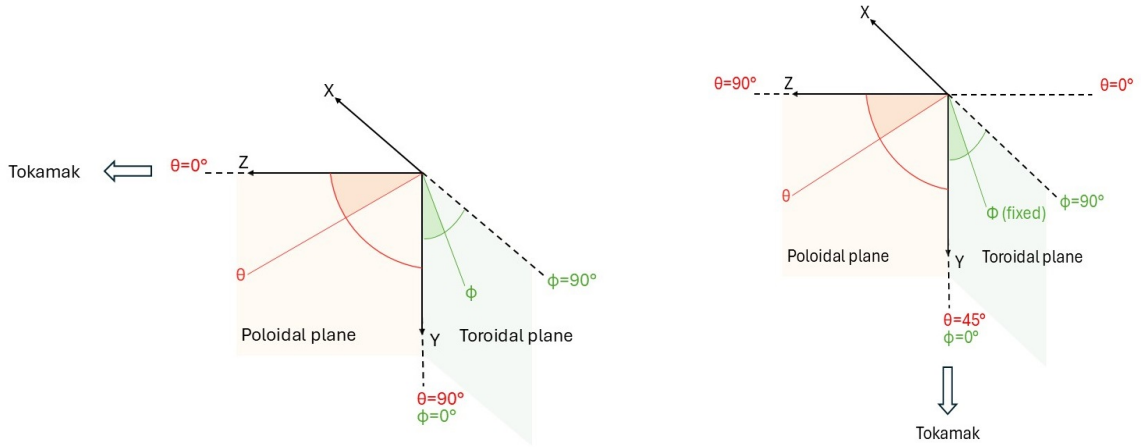

(a) Reference system for equatorial (L1, L4) and upper lateral (L2, L5) launchers.

(b) Reference system for top launchers (L10, L11).

Figure 3.7: Spherical coordinate systems used as a reference for the launchers. The cross section of the vessel lies on the poloidal plane of the launcher.

3.2 NBI system

While electron cyclotron waves injection remains the main mechanism for plasma heating and current drive in TCV, a further contribution is provided by the neutral beam injection system (NBI). The advantage obtained by the introduction of such a system is not limited to the achievement of higher temperatures: it also allows to obtain new plasma configurations, which can be very important in the understanding of plasma behaviors in the context of other nuclear fusion projects [26].

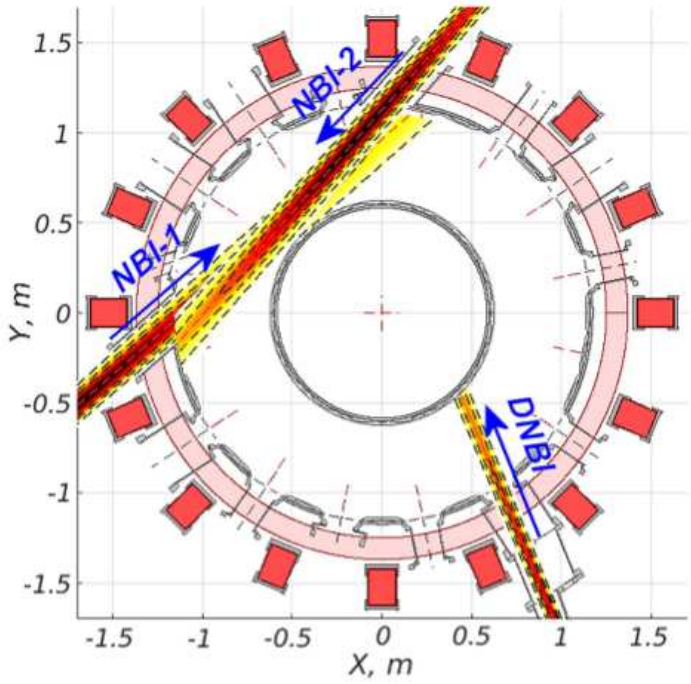

Figure 3.8: TCV neutral beam injectors scheme. Source: [27]

The injection of high ECRH power increases the electron temperature, but in low-density plasmas, since the thermal equilibration time of electron-ion classical Coulomb collision is significantly longer than the characteristic plasma confinement times, the ions temperature does not increase a lot, allowing only small ratios of ion to electron temperatures T_i/T_e. The main missions of TCV are to contribute to the physics basis for a more efficient exploitation of ITER and to the optimization of plasma scenarios and heating and control techniques in view of DEMO . This requires access to plasma regimes with high normalized plasma pressure, a wide range of ion/electron temperature ratios, including $T_i/T_e \sim 1$, a significant fast-ions population and relatively low collisionality [27]. Such conditions have been reached on TCV with the addition of a NBI system for direct ion heating: following ionization and charge exchange, fast atoms of the beam are trapped as plasma ions, and transport energy and momentum mainly to bulk ions, increasing their temperature.

The NBI system of TCV is composed of two neutral beam injectors, implemented respectively in 2015 and 2021, both D (deuterium) and H (hydrogen) compatible. The low-energy beam NBI-1 (28 keV in deuterium), mostly used for plasma heating, can inject a power of up to 1.3 MW, while the high-energy beam NBI-2 (52 keV in deuterium) can provide up to 1.1 MW of power in neutrals and is designed to operate with higher plasma densities and study fast-ion plasma interactions [27]. The two neutral beam injectors are directed in such a way that the neutral particles enter the vessel almost tangentially (the high-energy injector is counter-tangential to the plasma), as shown in Figure 3.8, where an additional neutral beam injector (DNBI) , used for diagnostics, is also present.

3.3 TCV operation

TCV is operated from Tuesday to Friday, with two scientific sessions per day. At the beginning of the first morning session of the week, a "stray" shot (from now on, the plasma pulses will be called *shots*) is performed to verify the proper operation of the coils. This consists of short, staggered current pulses applied sequentially to each shaping and transformer coil. Before the start of each morning session, glow discharge cleaning is performed for 30 minutes, followed by a test pulse to monitor the slow evolution of machine conditions over weeks and months. After this "standard" shot, the physics program starts.

During each session, multiple two-second shots are performed, typically one every 12 minutes. Between shots, glow discharge cleaning is usually performed again for approximately five minutes [28]. Each shot sequence begins in the control room, where the physics operator defines the plasma parameters. These parameters can be imported from a previously executed shot, if a specific plasma configuration needs to be repeated, and then adjusted as needed. Meanwhile, the gyrotron operator and the NBI operator set the parameters and waveforms for their respective systems, if their use is required for the shot. Once the necessary diagnostics for the experiment are configured, the pilot (the operator whose role is to run the shot) "fires" the pulse. After this point, no further interventions are possible. If the shot is successful, data are acquired by diagnostics, and post-processing codes are automatically run to elaborate the collected data. The results are then analyzed to determine the next shot.

All results are stored in a database, labeled with the sequential number assigned to each shot, and are available for further post-processing analysis, primarily using MATLAB. The work presented in the following chapters is largely based on the analysis of these data, utilizing both pre-existing codes and newly developed scripts.

Chapter 4

Methodology

The work carried out at the SPC in the context of this thesis is subdivided into two independent parts. Although the core idea was to develop a new tool to optimize the injection of EC waves into the plasma, an additional preliminary study was conducted to assess potential uncertainties in the mirror angles of launchers L10 and L11. The preliminary study aimed to quantify launchers' misalignment and their impact on microwave absorption. The details of this problem are presented in Chapter 5, while in the current Chapter only the methodology regarding the optimization of the EC injection angle is described, being the main focus of the thesis.

4.1 Motivation and objectives

As described in the previous chapter, TCV is equipped with a high-power Electron Cyclotron Resonance Heating & Current Drive (ECRH-ECCD) system, currently composed of three gyrotrons – two dual frequency and one second harmonic – which can inject microwaves through different launchers (see Figure 3.4 for possible configurations). The possibility of adjusting the power, frequency, and injection angle of the beams makes this system highly versatile, allowing adaptation to different plasma configurations and experimental objectives. To fully exploit this versatility, the choice of gyrotron parameters is crucial and should be defined individually for each shot, according to its specific goals.

This work focuses on optimizing the EC (Electron Cyclotron) wave injection angle, with the aim of increasing the efficiency with which the ECRH-ECCD system is used. As presented in Chapter 2, the absorption of EC waves in the plasma occurs only in a narrow region known as electron cyclotron resonance (ECR) layer, where the wave frequency matches the local electron cyclotron frequency. Because this layer is very thin, the interaction between the wave and the electrons is extremely sensitive to the direction in which the wave propagates through it. For instance, if waves are injected

from the top and in correspondence to the ECR layer, they stay inside this region for a longer distance, increasing the absorption probability. In contrast, if the waves are injected perpendicularly to this layer, the interaction time is much lower, making the energy transfer more difficult to occur. This explains why the choice of the correct injection angle is crucial to efficiently provide heating and current drive to the plasma.

Currently, the selection of the injection angle is primarily based on prior experience, which means that a new shot is usually configured by referring to a previously successful one, indicated as *reference shot*. Plasma parameters, as well as NBI and ECRH configurations, are typically loaded from this reference shot and eventually modified to explore new objectives. There is no true optimization process, being the angle chosen based on past successful cases and a trial-and-error approach. Moreover, since most experiments achieve to work with stationary plasmas, the angles are usually kept constant throughout the whole duration of the shot.

The objective of this work was to develop a tool capable of providing a qualitative estimation of the optimal launcher angles for a given shot and for a given objective, reducing in this way the dependence on previous experience. Once the goal of a new shot is defined and a reference shot performed in the past is identified, rather than simply replicating the injection angles of the reference shot or modifying them through a trial-and-error approach, a post-processing simulation can be performed on the data collected from the reference shot. This allows for an evaluation of whether different injection angles could improve a specific aspect – such as the fraction of absorbed power or the current driven in the plasma – within that particular plasma configuration. Since the simulation is computationally efficient, it can be executed in real time by the ECRH operator just before running the shot.

In particular, the possibility of using a time-dependent injection angle during a shot was explored, to determine whether it could provide sensible improvements in terms of efficiency compared to the constant-angle approach. This investigation is motivated by the fact that if certain plasma parameters change over time, the optimal injection angle might also need to be adjusted dynamically.

To implement the proposed optimization approach, a combination of existing analysis tools and newly developed scripts was used. The pre-existing tools provide a foundation for analyzing shot results, while additional post-processing codes were developed to extract relevant data and simulate different injection scenarios. The following section provides a brief description of the tools currently in use at the Swiss Plasma Center (SPC) for analyzing shot results.

4.2 Simulations codes

The analysis of shots data, stored in the database, is primarily conducted using the MATLAB software environment.

It is important to clarify a fundamental aspect of this type of analysis, which applies to all the work described in this thesis. In all of the codes used, the plasma equilibrium is reconstructed on the basis of a reference shot, and subsequent simulations are carried out on that specific equilibrium. This process does not include any feedback on the equilibrium itself, meaning that it remains unchanged from the original shot, regardless of how the simulated scenario differs from the reference. In other words, if the user simulates for example a situation with increased ECRH power compared to the reference shot, these scripts can provide information on how the rays would be absorbed in that specific equilibrium, but they do not take into account the increase of plasma temperature consequent to the introduction of the additional ECRH source. Considering also this effect would require solving a new plasma equilibrium, significantly increasing the complexity of the software from a physical point of view. Additionally, it would make the simulations highly time-consuming as a single run would take hours instead of seconds. The final aim of this work is to implement the developed optimization tool in the ECRH operator interface in the control room, allowing the operator to run the code before a shot to quickly obtain a qualitative estimate of the optimal angles values. Being the time between two shots, on a normal operation day, slightly over 10 minutes, an accurate simulation requiring several hours to complete would not be practical for the stated purpose. Of course, the drawback of this simplification is is a loss of accuracy, meaning that the results may significantly deviate from the real plasma behavior in some cases. This issue could be mitigated by iterating the process: after executing a new shot with the optimized angles for a certain scenario, an additional simulation could be performed to asses wether the obtained optimal angles align with the updated equilibrium. In the following, a brief overview of the scripts developed at SPC and utilized in this thesis is provided.

GUIprofs

GUIprofs is a GUI (Graphical User Interface) for shot analysis and preparation, developed in the MATLAB environment. It relies on multiple scripts to read from the database the plasma parameters – such as temperature and density distribution over the plasma radius – and to reconstruct the plasma equilibrium for a specific shot and time instant, given as input. Based on the equilibrium obtained, the user can simulate the injection of microwaves to analyze their interaction with the plasma. Here, there are two possibilities; in the first one, the microwave data are loaded from the database,

and in this case only the gyrotrons/launchers that were active during the real shot are simulated using the exact parameters applied in the experiment. In the second option, data are given as input from the user, allowing the simulation of microwave injection from other launchers and with different parameters, to see how they behave in that specific plasma equilibrium. In this case, the user must specify the active gyrotrons/launchers, the microwave frequency, and the injection angle.

Regarding the injection angles, GUIprofs has two modes of operation, depending on the format in which the simulated injection angles are given. In the *default mode*, for each active launcher a couple of angles is given – one for the poloidal and one for the toroidal planes of the launchers – defining in that way a unique injection direction for each launcher. The simulation of the microwave injection can be initialized directly from GUIprofs, which acts as an interface for providing the input data to the ray tracing software TORAY. TORAY automatically builds around this direction a set of rays, where the number can be changed defining it as input, using a Gaussian distribution, obtaining in this way a situation closer to the reality, where the beam can have a certain divergence. The other option is the *sweep mode*: in this mode, the user can define a custom distribution of rays, instead of the default Gaussian one. The user gives as input the angle range within which the beam will be distributed, as well as the number of rays, and GUIprofs automatically builds a spatial distribution. It is important to note that this spatial sweep can be done only in one of the two planes at time (poloidal or toroidal), while the other angle must remain fixed. An example of a microwave injection with poloidal sweep distribution is shown in Figure 4.1.

Another useful feature of GUIprofs, which will be used in the following, is the possibility to define custom launchers, allowing the user to specify the launchers position, the number of injected rays and their cone aperture.

In Figure 4.2 a screenshot of the GUIprofs interface is shown. The temperature and density distributions as well as the plasma boundary are displayed. The bottom-left image in the same figure illustrates the resonance regions for different frequencies (straight dashed lines), the magnetic surfaces (circular dashed lines), and the injected EC rays (solid straight lines). Once the plasma equilibrium is obtained and the desired scenario is set up, TORAY can be launched directly from the GUIprofs interface to calculate the propagation of EC beams inside the TCV vessel.

TORAY

TORAY is a ray-tracing code written in Fortran 90, used for electron cyclotron heating and current drive simulations [29]. The ray tracing algorithm uses a modified Adams method to follow the trajectory of rays in the electron cyclotron frequency range, as they propagate through the plasma, computing absorption and current driven. To de-

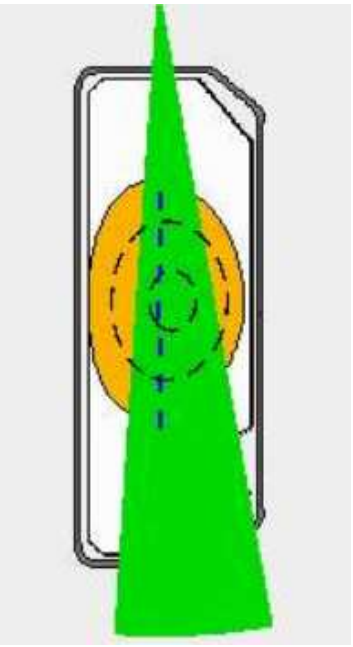

Figure 4.1: Microwaves injection in the TCV vessel, with rays uniformly distributed on the poloidal plane. Rays are injected from L11 and space in the interval between 40° and 47°. Realized with the sweep mode of the GUIprofs interface.

termine the absorption along the ray path, several damping models are available, which solve the dispersion relation in the cold or warm plasma approximation in the vicinity of a desired harmonic. The electron cyclotron current drive is computed including relativistic effects, electron-ion collisions, and trapped particle dynamics. TORAY can simulate the injection of a set of rays with a given shape (e.g. Gaussian), defined as input.

Toray_automatic

Toray_automatic is a tool developed at SPC to automate the use of TORAY. Its functionality is similar to that of GUIprofs, with the difference that there is no graphic interface. Among all the possible toray_automatic inputs, users can specify the shot to analyze, the active launchers, the number of injected EC rays and their injection angle. Similarly to GUIprofs, toray_automatic allows for the simulation of EC ray injection with a spatial sweep. In this case, the angle distribution must be built in advance, in order to provide toray_automatic with the injection angles for the single rays. The frequency and the power of the gyrotron can be either set manually or assigned default values.

Toray_automatic allows for multiple parallel runs of TORAY, at different time frames, enabling the simulation of EC absorption over the entire duration of a shot. This makes it more versatile than GUIprofs for a time-dependent optimization, as

GUIprofs only allows simulations for a single time frame at a time.

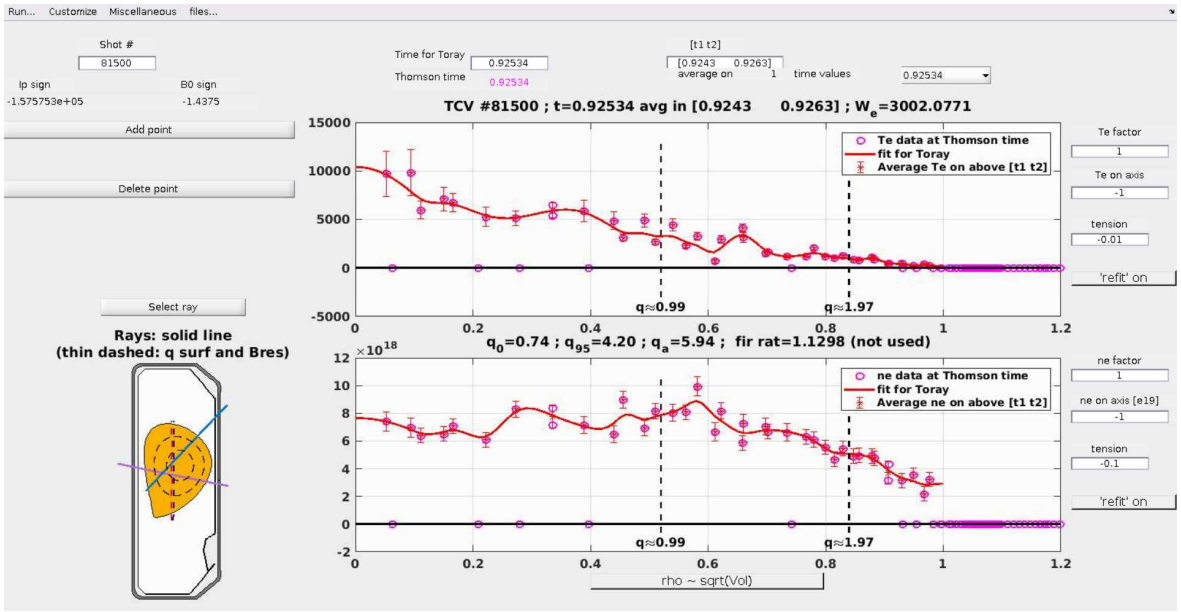

Figure 4.2: GUIprofs interface for shot 81500, with EC waves injection from launchers L1, L4 and L5.

4.3 Implementation of the EC waves injection optimization

The aim of this work was to develop a tool capable of defining the best injection angle for a certain EC launcher, for a given plasma scenario. EC waves can be used for both plasma heating and current drive, so the possibility to optimize both aspects was implemented, giving the user the possibility to choose.

The developed tool, named Angle_opt, is based mainly on toray_automatic, and exploits its possibility to run multiple simulations in parallel. In particular, this feature is used to optimize the angle at multiple time instants in order to obtain an optimal angle which is a function of time. This can be relevant in the case of plasmas with changing properties over time.

The inputs required to run the code are the same as those needed by toray_automatic, with the difference that the input injection angle should be a spatial distribution, not a single one. The optimization is indeed based on the sweep mode described previously: the user defines for each launcher a range of angles inside of which the optimal value must be found, and the code constructs a beam of rays with a uniform distribution inside of this range, where the number of rays can be defined as input. It should be noted that the distribution of rays can be either in the poloidal or toroidal direction,

meaning that one of the two angles defining the injection trajectory must be maintained constant. The spatial distribution is then provided as input to TORAY, which computes the percentage of power absorbed by the plasma and the current driven by each ray. Subsequently, the code interpolates the obtained results and it searches for a global maximum of the quantity to optimize inside of the input angles range. If the range was chosen carefully, the function finds this maximum, and it returns the value of the optimal angle value corresponding to the maximum. This process is parallelized for multiple time steps, which can be defined by the user by choosing the time interval to analyze.

Although the tool was mainly thought to optimize plasma heating and current drive, a third optimization option was added. For certain shots it might be useful to deposit power at a specific radius, rather than maximizing the overall absorption inside of the plasma; this is true in the case of instabilities, which can be dumped by injecting power in the proximity of the region where these instabilities rise. The script was designed so that the user can define as input the magnetic surface of the plasma at which the EC power should be deposited. The code launches TORAY, and then for each ray of the spatial distribution it reads the percentage of power which is deposited at the radius corresponding to the target magnetic surface. As for the other parameters, the script interpolates the obtained values and it returns the angle which maximizes the power deposition in the target position.

Regardless of the parameter selected for the optimization, the output of the analysis is a set of curves showing the optimal injection angle as a function of time for each active launcher defined by the user. Active launchers can perform sweeps in different directions and can optimize different aspects independently. An example of the resulting curves is shown in Figure 6.2, where the dashed lines in the right plot represent the range of angles that deviate from the optimum by less than $\pm 5\%$ of the maximum value of the optimized parameter. This plot alone fulfills the objective of the analysis, without requiring further data elaboration: it provides a qualitative estimation of how far the injection angles used in the reference shot are from the theoretical optimal ones, enabling the EC operator in the control room to adjust the injection direction of EC waves based on the optimization results and the objective of the next shot.

Different shots were performed, in order to test the Angle_opt optimization tool in different scenarios. The description of the experiments and the results obtained are presented in Chapter 6.

Chapter 5

Launchers Geometry Correction

Prior to the work presented in this thesis, a discrepancy was observed between the predictions made by TORAY and the experimental results regarding the absorption of microwaves injected from the two X3 top launchers (L10 and L11). For example, in certain shots TORAY predicted a complete absorption of a microwave beam, whereas in reality some unabsorbed rays were detected from specific sensors placed on the vessel. This discrepancy suggested a possible misalignment of the X3 mirrors, leading to a deviation between the expected and actual injection directions of the beams.

5.1 Correction through injection angle adjustment

In the past, a series of shots was performed to prove the misalignment of the X3 mirrors and eventually quantify the discrepancy. The idea was to analyze how the power absorption in the plasma changed while varying the poloidal angle of the injected beam (this cannot be done for the toroidal angle, being fixed for these launchers) and to compare the resulting curve with the one obtained from a TORAY simulation. For both curves a peak was expected, corresponding to the optimal angle that maximizes absorption. If the mirrors were not perfectly aligned, a shift between the peaks of the two curves would be observed, indicating that the actual injection direction differed from the expected one.

To collect data on real power absorption, DMPX (Duplex Multiwire Proportional X-ray Counter) and electron temperature diagnostics were used as indirect measures of the absorbed power, considering that an increase in power absorption would lead to a rise in plasma temperature. During the shots, the poloidal angles of L10 and L11 were changed over time, while temperature measurements were recorded, obtaining a relation between power absorption and injection angle. Then, TORAY was run in sweep mode to simulate ray injection at different poloidal angles simultaneously, calculating for each of them the fraction of power absorbed by the plasma.

The comparison between experimental and simulated curves revealed an offset between their peaks, confirming the misalignment of the mirrors of the two launchers: the launchers injected power in a direction slightly different from the one defined from the operator, introducing the constant offset which was observed between the two curves. This offset was quantified to be -0.3° for L10 and -0.4° for L11, where the sign indicates that the experiments underestimate the optimal angle, compared to the post-processing simulation with TORAY. Knowing the error affecting the angle of the L10 and L11 mirrors, a correction was introduced on the ECRH operator interface, in such a way that when a certain angle is given as input to the launchers, the system automatically corrects the estimated offsets, so that the launchers point in the desired direction.

5.2 Validation of the injection angle correction

The described correction worked reasonably well for most shots, but for others it seemed to be less precise, as if the offsets were not constant but were influenced by other unknown parameters. To further investigate on this problem, two shots were performed, labeled with the numbers 83816 and 83883. The main difference between the two shots was the vertical position of the plasma axis z_{axis} (where z_{axis}=0 means that the plasma is centered with respect to the height of the vessel):

- shot 83883: $z_{axis} = 5$ cm
- shot 83816: $z_{axis} = 23$ cm

During these shots, launchers L10 and L11 were switched on alternatively, the first in the interval between 0.3 and 0.8 s and the second between 0.8 and 1.3 s. The launcher poloidal angles θ were gradually changed between 44° and 45.5°, while the electron temperature in the plasma was measured. In this way a correlation between injection angle and electron temperature – and so also with the power absorption – was obtained, and was then compared with the fraction of absorbed power simulated by GUIprofs, exactly as it was done to quantify the mirrors' displacement in the first place. In Figures 5.1 and 5.2 this comparison is shown for L10 and L11, for both shots. In these plots, the offset correction was removed, to highlight the difference between simulation and real data, consequent to the misalignment of the mirrors.

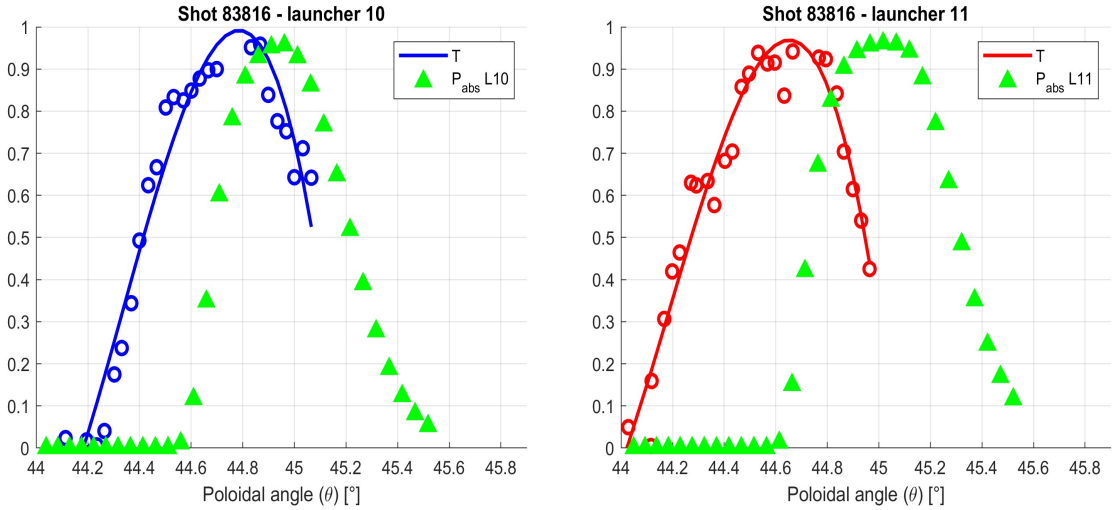

(a) P_{abs} and T vs poloidal angle θ, for L10. **(b)** P_{abs} and T vs poloidal angle θ, for L11.

Figure 5.1: Comparison between electron temperature (measured) and fraction of absorbed power (calculated with GUIprofs) as function of the poloidal angle, for shot 83816. No angle correction is applied: an offset between the two peaks is evident.

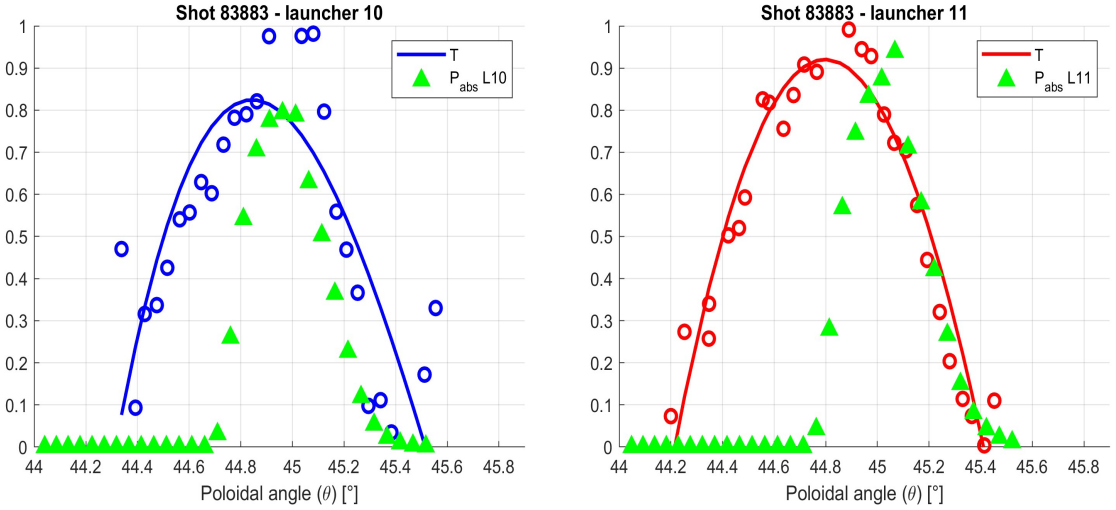

(a) P_{abs} and T vs poloidal angle θ, for L10. **(b)** P_{abs} and T vs poloidal angle θ, for L11.

Figure 5.2: Comparison between electron temperature (measured) and fraction of absorbed power (calculated with GUIprofs) as function of the poloidal angle, for shot 83883. No angle correction is applied: an offset between the two peaks is evident.

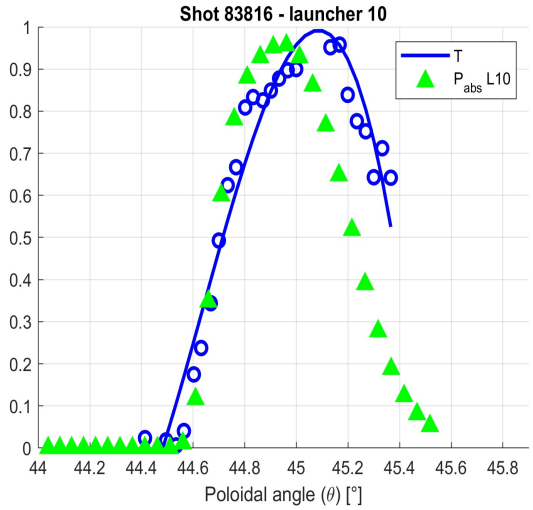

(a) P_{abs} and T vs poloidal angle θ, for L10.

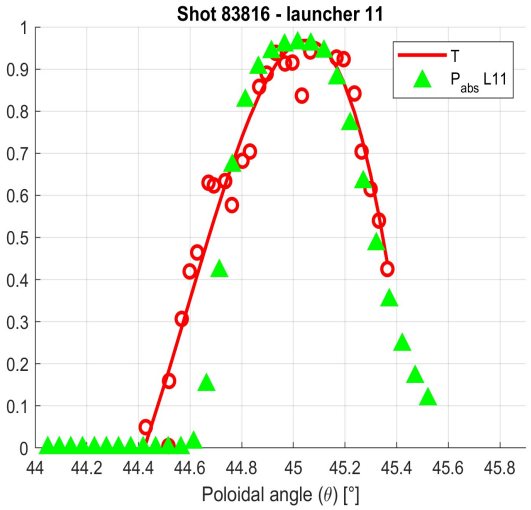

(b) P_{abs} and T vs poloidal angle θ, for L11.

Figure 5.3: Comparison between electron temperature (measured) and fraction of absorbed power (calculated with GUIprofs) for shot 83816, with angle correction.

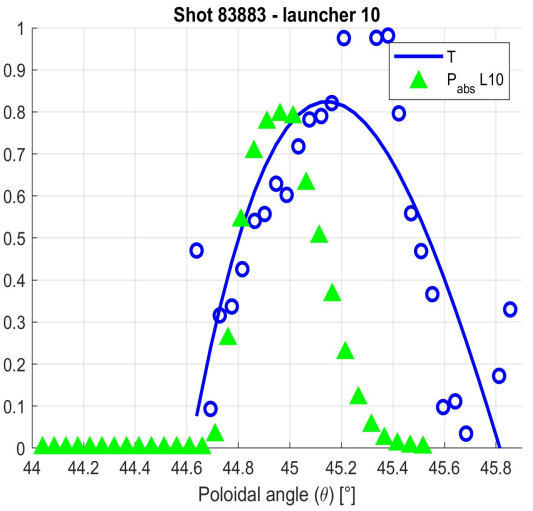

(a) P_{abs} and T vs poloidal angle θ, for L10.

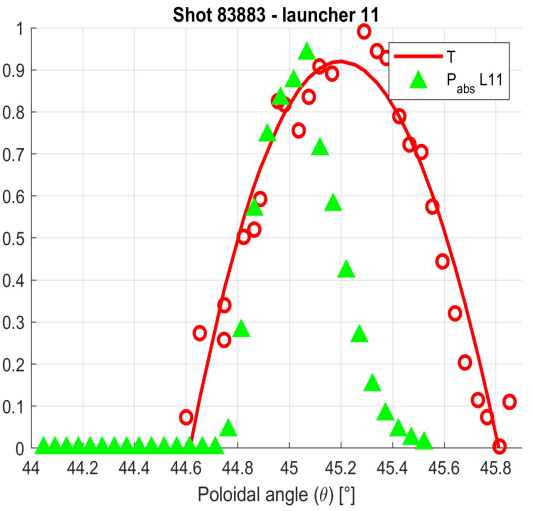

(b) P_{abs} and T vs poloidal angle θ, for L11.

Figure 5.4: Comparison between electron temperature (measured) and fraction of absorbed power (calculated with GUIprofs) for shot 83883, with angle correction.

The temperature curves were obtained by considering only the temperature in an area close to the center of the plasma. Starting from the raw data, a baseline temperature level was subtracted in order to underline the effect of the ECH on the temperature. The data were then normalized with respect to the maximum temperature, in order to obtain a relative curve, and subsequently interpolated.

The curves representing the fraction of absorbed power were obtained giving as input to GUIprofs a uniform ray distribution between 44° and 45.5°, considering a single time frame. An inaccuracy is introduced by the fact that the spatial sweep of the launchers simulated with GUIprofs considers the plasma equilibrium in a single time instant, while in the actual experiment the launchers were moved over time. Consequently, the temperature data were measured at different times and may be influenced by potential variations in plasma parameters. To mitigate this issue, an effort was made to keep plasma properties as stable as possible during the shots. This ensured that comparing the temperature measurements, dependent on time, with the power absorbed at different angles calculated using GUIprofs introduced minimal inaccuracies.

An offset between the two curves of Figures 5.1 and 5.2 is evident, confirming the mirrors misalignment described earlier. In Figures 5.3 and 5.4 the same curves are shown, but the offset correction is now reintroduced, resulting in a shift toward right of the electron temperature curves. It can be seen that, for both launchers, the angle correction works reasonably well for shot 83816, while it seems to overcorrect the angle for shot 83883, resulting in a shift between the power and temperature curves in the opposite axis direction. The z-coordinate of the plasma axis is the main difference between the two shots, suggesting that the discrepancy between experiments and simulations may be a function of this parameter, rather than constant as was considered before. A correction taking into account the variability of the discrepancy with the z-coordinate of the plasma can be introduced if an uncertainty on the radial position of the launchers is assumed, having that an error on this parameter would reflect on an error on the injection angle which decreases at lower plasma positions.

5.3 Correction through launchers position adjustment

Assuming for simplicity that the optimal injection angle for a given launcher is the one that allows the beam to reach the center of the plasma, any discrepancy between the expected and actual radial position of the mirror would lead to a difference between the ideal (TORAY) and the real optimal mirror angles, as illustrated in Figure 5.5.

Taking Figure 5.5 as a reference, in the presence of a mismatch between the ex-

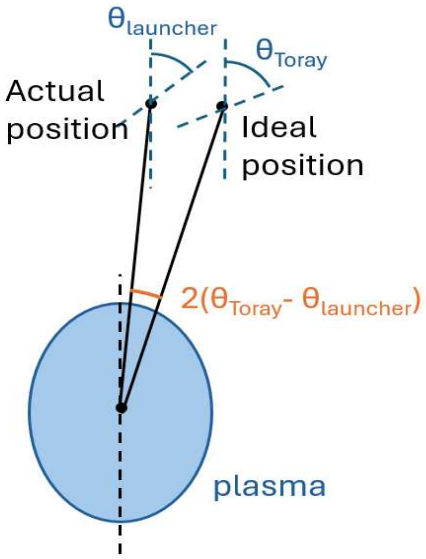

Figure 5.5: Difference between ideal and real optimal microwave injection angles in the case of an uncertainty on the radial position of a launcher.

pected and actual radial position of the launcher, the peak of power absorption in the experiments would appear at lower angles compared to the simulations, resulting in the observed discrepancy between experimental and simulated results. Following this new approach, the discrepancy is now a function of z_{axis}, since the difference between the ideal and actual injection angles decreases as the plasma moves farther from the launcher.

This explanation would justify why the correction applied so far is effective for shots with a high z_{axis}, but tends to overcompensate the observed offset for plasmas closer to the bottom of the vessel, as in shot 83883.

5.4 Validation of the launchers radial position correction

To prove what just presented, it was necessary to quantify the effect of the radial position of the launchers on the estimation of the optimal injection angle. This was done using GUIprofs, thanks to a functionality which allows the definition of fictitious launchers with custom parameters and positions. Simulations were performed with these newly defined launchers, changing their radial position while maintaining all other parameters the same. Figure 5.6 shows the power absorption as a function of the injection angle for different radial positions of the L11 launcher. In the GUIprofs reference system, the radial position corresponds to the x coordinate, and the following

values were tested:

- x = 0.85 cm (default)
- x = 0.86 cm
- x = 0.84 cm

Only the curves obtained for L11 are presented here, having for L10 an analogous situation.

Figure 5.6 clearly demonstrates that even minor deviations in the radial position of the launchers can significantly affect the optimal angle resulting from the experiments. Moreover, this effect is more pronounced for shot 83883, which is consistent with the observation that the discrepancy between simulated and experimental optimal angles decreases for plasmas located closer to the bottom of the vessel.

Based on this result, a TORAY simulation was performed on shot 83816 (z_{axis} = 23 cm), modifying the launchers position to qualitatively match the two curves of Figure 5.1 – the temperature measured in the experiments and the absorbed power simulated with TORAY – for each launcher. The match was achieved by applying the following shifts to the launchers radial position:

- -0.5 cm for L10
- -0.8 cm for L11

The new curves obtained with these shifts for shot 83816 are shown in Figure 5.7.

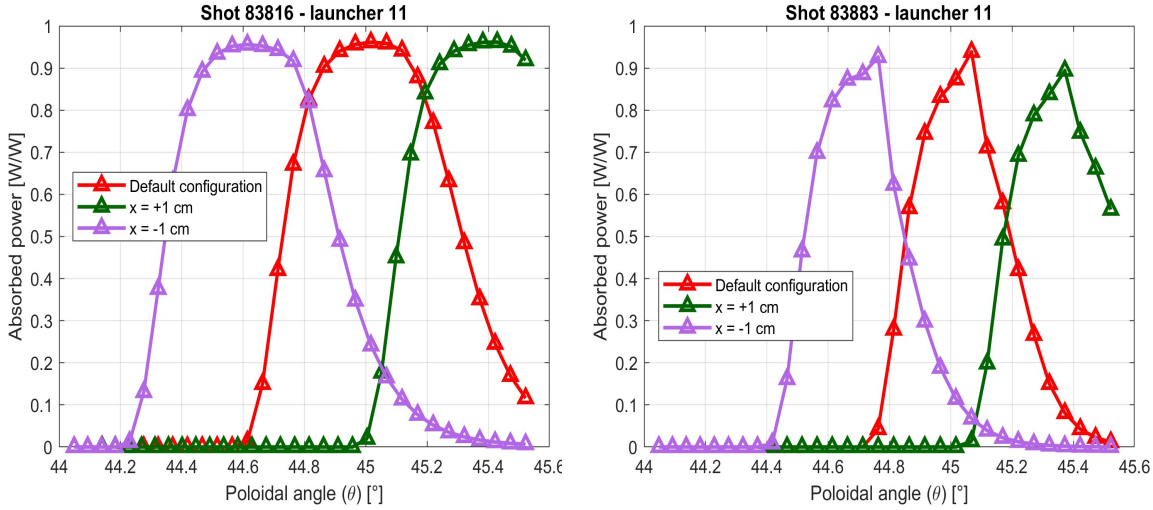

(a) P_{abs} vs poloidal angle θ, for shot 83816. **(b)** P_{abs} vs poloidal angle θ, for shot 83883.

Figure 5.6: Simulation of power absorption for different radial positions of launcher L11, for shots 83816 and 83883. The curves were obtained from GUIprofs simulations.

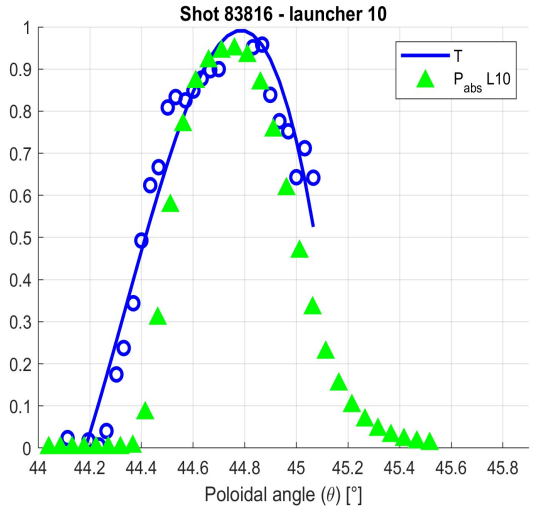

(a) P_{abs} and T vs poloidal angle θ, for L10.

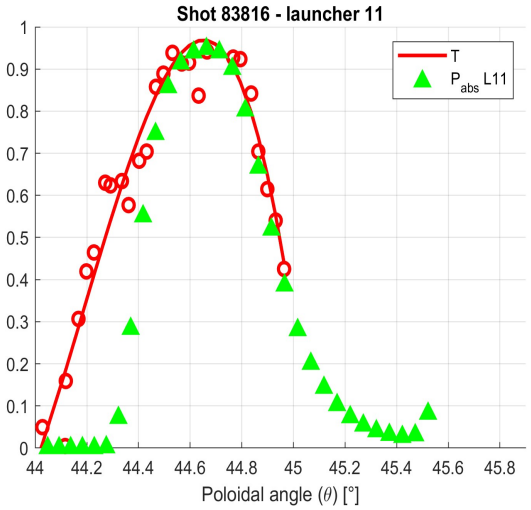

(b) P_{abs} and T vs poloidal angle θ, for L11.

Figure 5.7: Comparison between electron temperature (measured) and fraction of absorbed power (calculated with GUIprofs) for shot 83816, with angle correction.

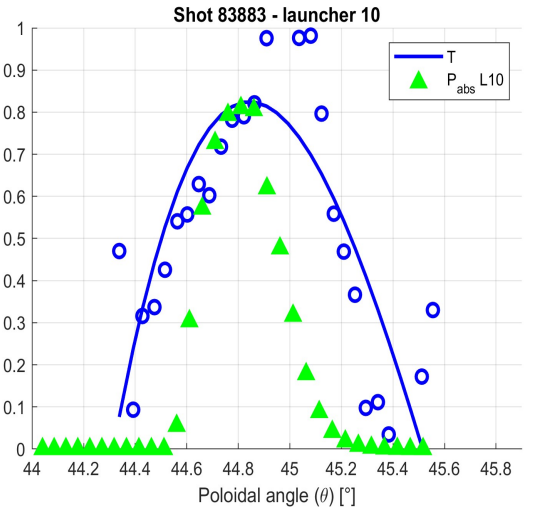

(a) P_{abs} and T vs poloidal angle θ, for L10.

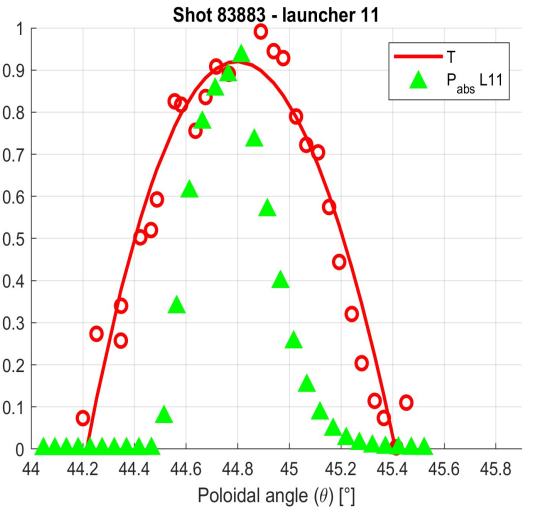

(b) P_{abs} and T vs poloidal angle θ, for L11.

Figure 5.8: Comparison between electron temperature (measured) and fraction of absorbed power (calculated with GUIprofs) for shot 83883, with angle correction.

To confirm that a correction based on the launchers' radial position works better than the one based on an angle correction, used so far, the same shifts obtained for shot 83816 were applied to the launchers in a new simulation of shot 83883, to see if this correction works even on a plasma with a lower z-coordinate. The curves shown in Figure 5.8 demonstrate that the offsets in the position of the launchers, determined

for 83816, also work for shot 83883, allowing the measured temperature peaks and the simulated absorbed power to match.

5.5 Conclusions

If the discrepancy between experiments and simulations in the definition of the optimal EC wave injection angle for L10 and L11 is addressed by introducing a correction which considers a misalignment of the mirrors, as done so far, the observed mismatch is sensibly reduced. However, this may not be true for all the cases, as it has been observed that for plasmas close to the bottom of the vessel, this type of correction tends to overestimate the gap between experimental and simulated results. This led to the hypothesis that a correction dependent on the z-coordinate of the plasma axis could be more appropriate. The dependency on the z-coordinate can be accounted for by assuming an error on the launchers radial position, which was quantified to be 0.5 cm for L10 and 0.8 cm for L11. From what was presented in this chapter, a correction based on the assumption that the radial position of the launchers may be affected by an uncertainty seems to be more precise than simple mirrors angle adjustment.

The purpose of this study was to illustrate a new possible approach only qualitatively, and it was carried out for a limited number of shots; therefore, the values found here are likely to be imprecise. A confirmation based on other cases with different parameters, and especially different values of z_{axis}, may be needed, also to understand whether other parameters can have an impact on this gap between experimental data and simulations. Moreover, it cannot be excluded that the observed discrepancy is the result of both a misalignment of the angle of the mirrors and an uncertainty in the exact radial position of the launcher, rather than the latter alone. Further investigations should take both factors into account.

Chapter 6

Optimization of the EC Wave Injection Angle

In Chapter 4 the working principles of the EC optimization tool developed in the framework of this thesis were introduced. The purpose of the current chapter is to present the results obtained from using this script. Specifically, the Angle_opt tool was tested through the optimization of the injection angles in two different scenarios: one aimed at maximizing the power absorbed by the plasma, presented in Section 6.1 and another focused on optimizing the current drive, in Section 6.2.

The general workflow followed in both cases is outlined below. First, a target shot was identified, based on the goal of optimizing either power absorption or current drive. A new plasma discharge with the same characteristics was then performed, in order to obtain updated data on the non-optimized case. This newly performed discharge served as the reference shot. Angle_opt was then executed on this reference case, in order to determine the optimal EC wave injection angles for the given plasma conditions.

Once the optimal angles – expressed as a function of time – were estimated for all active launchers, a new experiment was set up with the same plasma characteristics as the reference shot, but using the optimized injection angles instead of the original ones. Data from this new experiment were then collected and compared with those of the reference case to see if the usage of the EC optimization tool could lead to measurable improvements in EC wave injection.

Additional experiments and considerations specific to each scenario are discussed in the corresponding sections.

6.1 Optimization of power deposition

The reference scenario selected for the optimization of overall EC wave absorption is shot number 82313, an experiment originally conducted for different purposes. The

peculiarity of this scenario is the downward shift of the plasma during the discharge, bringing it closer to the bottom of the tokamak. As a result of this change in position, the optimal injection angle is expected to vary over time to adapt to the changing plasma geometry. This makes it an optimal test case for evaluating the performance of Angle_opt in a dynamic context.

6.1.1 Description of the experimental shots

This section provides a detailed description of the experiments carried out to test the Angle_opt optimization tool.

Shot 84889

A new shot – labeled 84889 – was performed with the same exact characteristics as shot 82313, to have more recent data regarding the reference scenario. In the original configuration, only ECRH was employed as an external heating source (ohmic heating from the plasma current was still present): 800 kW of microwaves at the third harmonic (X3) were injected by launcher L11 between 0.3 s and 1.5 s, taking the plasma breakdown as the initial reference point for the times. The injection direction was kept constant throughout the discharge, with a toroidal angle (ϕ) of -2.59° and a poloidal angle (θ) of 44.85°. These values are defined according to the launcher reference system shown in Figure 3.7b. During the discharge, the height of the plasma axis decreased from 22 cm to 0 cm, as shown in Figure 6.1. All input data related to this and the subsequent shots are summarized in Table 6.1.

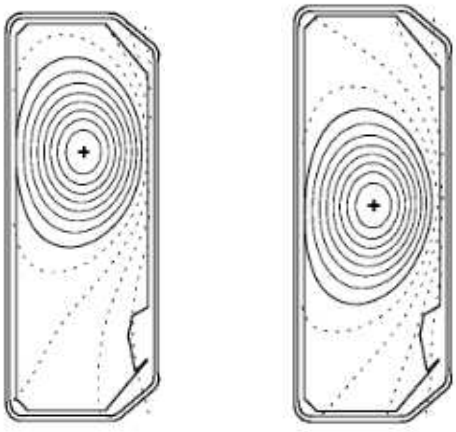

(a) Plasma position at 0.2 s.

(b) Plasma position at 1.4 s.

Figure 6.1: Plasma position at different times during shot 84889.

Shot 84891

A second experiment – shot number 84891 – was then performed, varying the poloidal angle of launcher L11 over time. The purpose of this experiment was to highlight the strong impact of the injection angle on the EC power deposition. EC injection began at 0.3 s with an initial poloidal angle of 44.5°, which was linearly increased to 45.2° by 0.9 s. It was then linearly decreased back to the initial value of 44.5° by 1.5 s. After this point, the microwave injection was interrupted due to plasma disruption. The evolution of the poloidal angle during discharge is shown in Figure 6.3b.

Shot 84818

At this point, the Angle_opt optimization script was run on shot 84889 to determine the injection that maximizes power deposition for the specific plasma equilibrium.

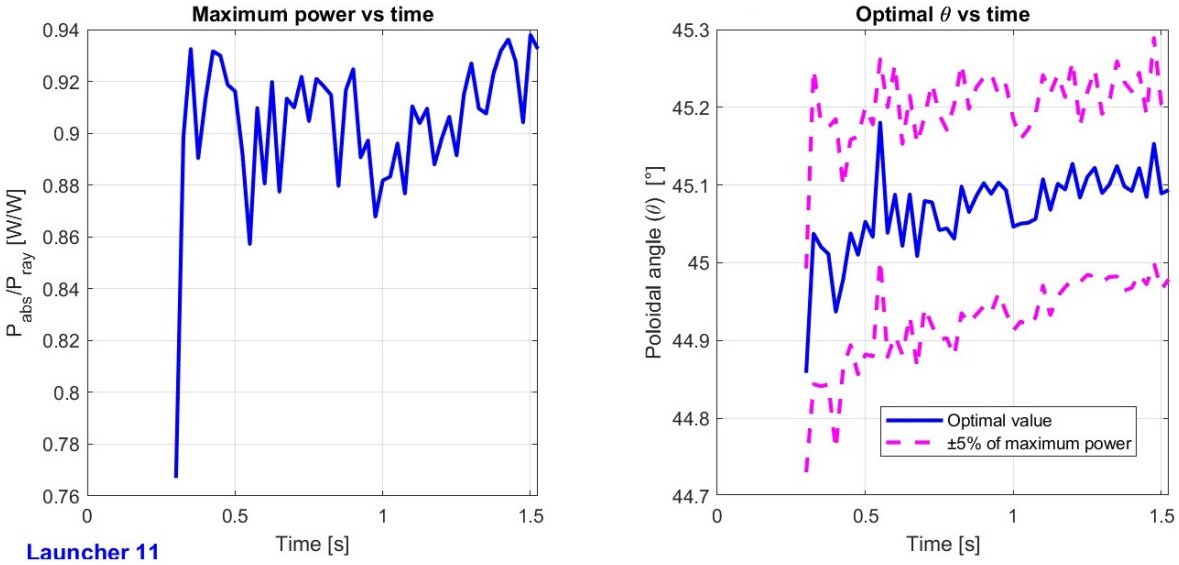

Figure 6.2: Results of the optimization of EC power deposition for shot 84889.

Figure 6.2 shows the results of the EC power absorption optimization. The right-hand graph represents the optimal angle as a function of time, along with two dashed curves indicating the angle range within which the absorbed power remains within ±5% of the maximum value. It can be seen that the optimal angle slightly changes over time, approximately from 45° to 45.1°, confirming the fact that with geometry changes in the plasma it might be opportune to adopt a microwave injection which changes over time if one wants to optimize the power absorption. The left-hand graph of Figure 6.2 shows the fraction of power absorbed by the plasma when the optimal injection angle is adopted.

Finally, one last experiment – shot number 84818 – was performed by injecting power using the optimized injection angle. The poloidal angle of launcher L11 was

gradually changed over time, starting from 45.05° at 0.3 s and reaching 45.1° at 1.5 s.

Table 6.1: Input data of the shots performed for the optimization of ECRH.

Shot number	Power from L11 [kW]	Theta [°]	Phi [°]	ECRH times [s]
84889	800	44.85	-2.59	0.3 → 1.5
84891	800	44.5 → 45.2 → 44.5	-2.59	0.3 → 0.9 → 1.5
84818	800	45.05 → 45.1	-2.59	0.3 → 0.8

6.1.2 Comparison between the shots

In total, three experiments were carried out. The first one, shot 84889, served as the reference case, with a constant and not non-optimized EC injection angle. Shot 84891 was then performed to investigate how the absorbed power varies with different injection angles. Lastly, shot 84818 adopted the optimized angle, in order to demonstrate the effectiveness of the optimization tool developed in the context of this thesis. Figure 6.3 shows the poloidal angle of launcher L11, measured during the experiments.

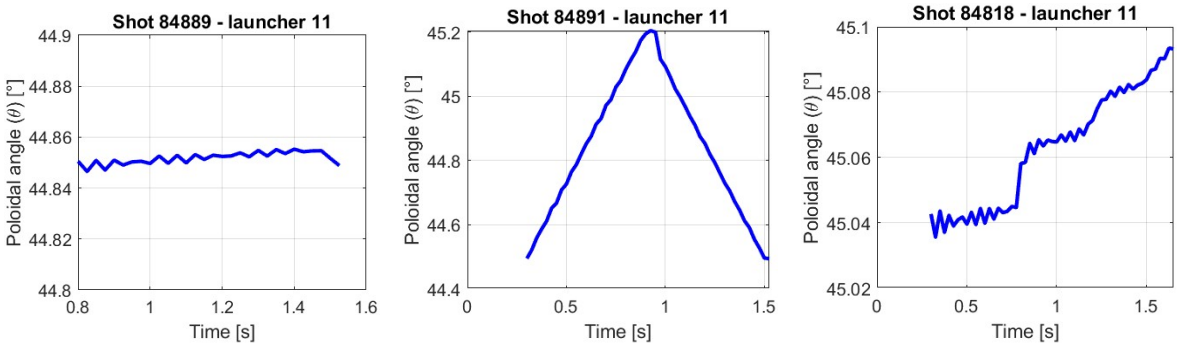

(a) Shot 84889. **(b)** Shot 84891. **(c)** Shot 84818.

Figure 6.3: Poloidal angle of launcher L11 measured during the three experiments.

To assess whether the use of the optimal injection angle effectively enhanced EC power absorption, a comparison between the power measurements of the three shots would be ideal. However, it is not possible to directly measure the fraction of EC power absorbed by the plasma. An indirect estimate can be obtained by taking into account the electron temperature data, considering that higher absorption efficiency leads to an increase in plasma temperature. Figure 6.5 shows the temperature measurements for the three shots, along with their respective interpolation curves. The plotted values represent the average temperature across the entire minor radius of the plasma and are displayed as a function of time. The temperature profile of shot 84818 shows an

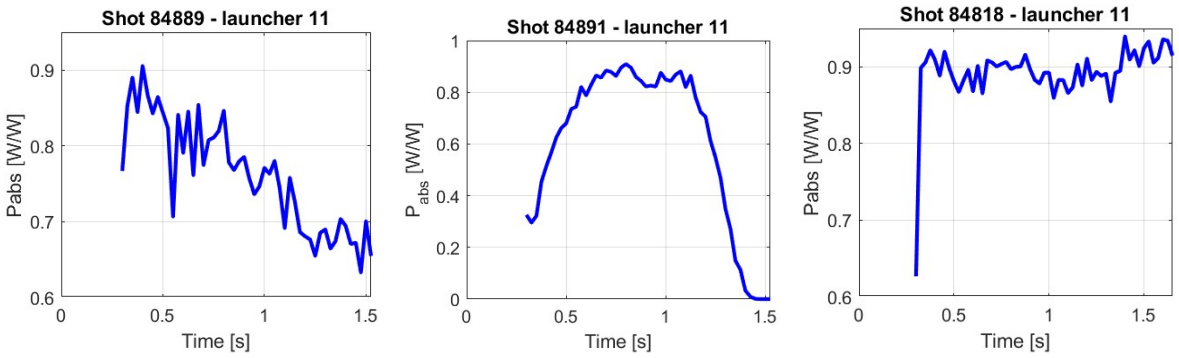

(a) Shot 84889. **(b)** Shot 84891. **(c)** Shot 84818.

Figure 6.4: Percentage of power absorbed in the three experiments, simulated with toray_automatic.

improvement compared to shot 84889, confirming the effectiveness of the optimization tool. The third curve represents the plasma temperature of shot 84891 and highlights the correlation between plasma temperature and injection angle – having a trend that follows the angular variation shown in Figure 6.3b – confirming in this way the possibility of having an estimate of the power absorption by considering electron temperature data. Naturally, this approach comes with limitations. The electron temperature is supported not only by ECRH, but also by ohmic heating generated by the plasma current. The effect of the two mechanisms cannot be separated in the measurements; the consequence is that the resulting temperature differences between the shots remain relatively small, since regardless of the absorption efficiency, the plasma current continues to sustain the temperature.

A more direct estimation of the absorbed power can be achieved through numerical simulations with TORAY, which can directly calculate the percentage of ECH power absorbed by the plasma in each scenario. For this purpose, toray_automatic was executed on all three shots. Figure 6.4 shows the absorbed power over time computed in this way. In the case with a constant injection angle, a clear decrease in power absorption can be observed over time, confirming that changes in plasma geometry lead to a less efficient absorption process if the injection angle is kept fixed over time. The second case further confirms that the variation of the poloidal angle has a significant impact on power absorption, which follows a trend consistent with the angle's time evolution. Finally, a sensible improvement is achieved when a time-dependent optimization of the injection angle is implemented, as shown in the plot regarding shot 84818, where the fraction of absorbed power remains nearly constant throughout the duration of the experiment.

Qualitatively, the graphs in Figure 6.4 show a behavior analogous to the experimental results presented in Figure 6.5. Based on these observations, it can be concluded

that the use of the Angle_opt optimization tool led to an improvement in the overall power absorption for this specific scenario.

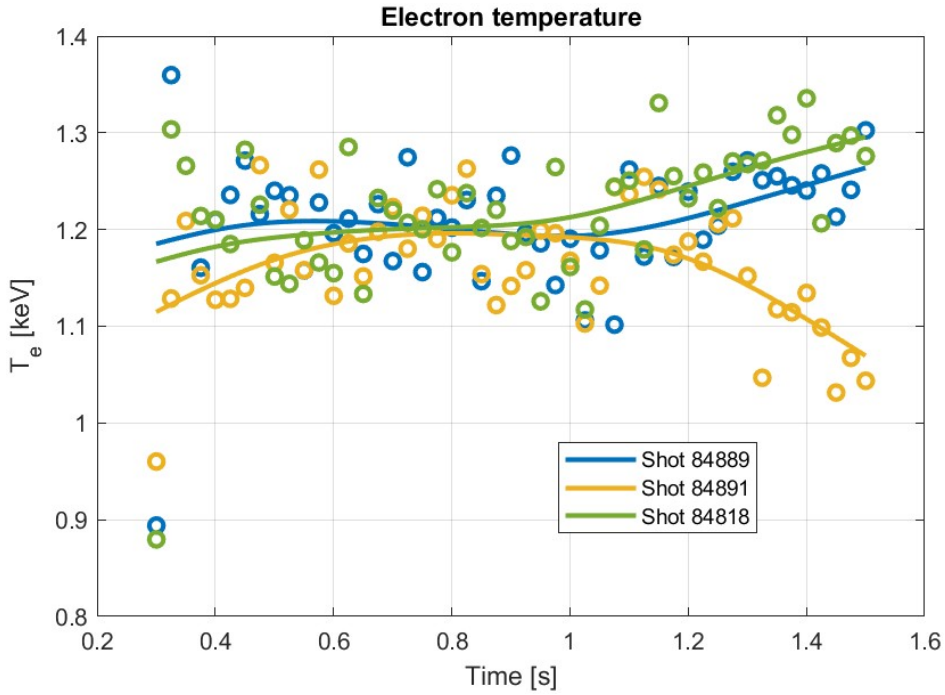

Figure 6.5: Electron temperature measures for shots 84889, 84891 and 84818.

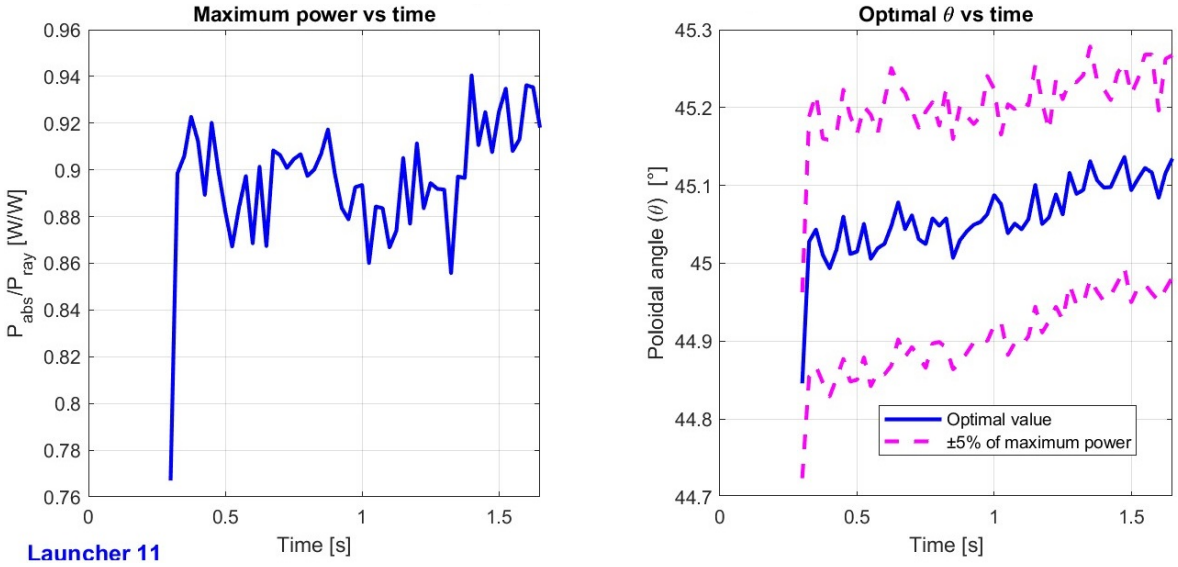

Figure 6.6: Results of the optimization of EC power deposition for shot 84818.

At this point, one last consideration should be made. As described in Section 4.2, plasma parameters, such as temperature and density, affect the optimal launcher angle that maximizes EC power absorption. The reverse is also true: changes in the injection

angle of EC waves influence the plasma equilibrium, potentially altering temperature and density values, and consequently shifting the optimal injection angle. This mutual dependence is not taken into account in the implementation of toray_automatic, which bases all the analysis on a given plasma description, without incorporating any type of feedback when the injection of EC waves is changed. As a result, the computed optimization may be valid for the initial plasma equilibrium but not necessarily accurate once the EC injection angle has been adjusted. A possible solution to this limitation is to iterate the process, re-running Angle_opt on the updated equilibrium to assess whether the optimal angle has changed due to the modified plasma conditions. Figure 6.6 shows the optimization results for shot 84818. The curves are nearly identical to those in Figure 6.2, corresponding to shot 84889, indicating that in this case changes in the plasma parameters have little impact on the optimal angle. This justifies, in this case, the use of a tool with no feedback control.

6.2 Optimization of current drive

Shot number 81500 was selected as a reference scenario to test the Angle_opt tool in the optimization of the current drive. It was chosen because its objective was to achieve fully non-inductive current drive in the plasma: after the initial breakdown, the central solenoid of the tokamak was turned off, leaving ECCD and NBI as the only mechanisms responsible for sustaining the total plasma current. The absence of the ohmic component of the current, normally induced by the transformer-like action of the central solenoid, made this scenario ideal to highlight the importance of a proper choice of the EC wave injection angle.

6.2.1 Description of the experimental shots

The experiments performed in the context of ECCD optimization are presented in the current section.

Shot 81500

Shot 81500 was chosen as the reference shot. At the beginning of the discharge, the ohmic current was required in order to initiate the plasma, but was turned off after 0.9 s, to let the NBI and ECCD systems drive a fully non-inductive current. The NBI system was primarily used to heat the plasma later in the discharge, in order to maintain a stable temperature. Only the NBI-1 unit was employed, starting the injection of neutral particles at approximately 1.2 s. The power injected by the different systems, along with their respective working times, is shown in Figure 6.7.

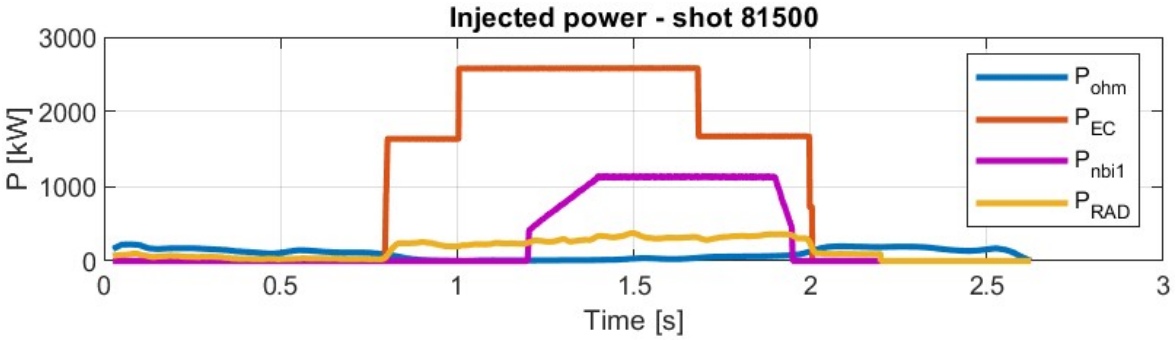

Figure 6.7: Power injected by the different systems during shot 81500.

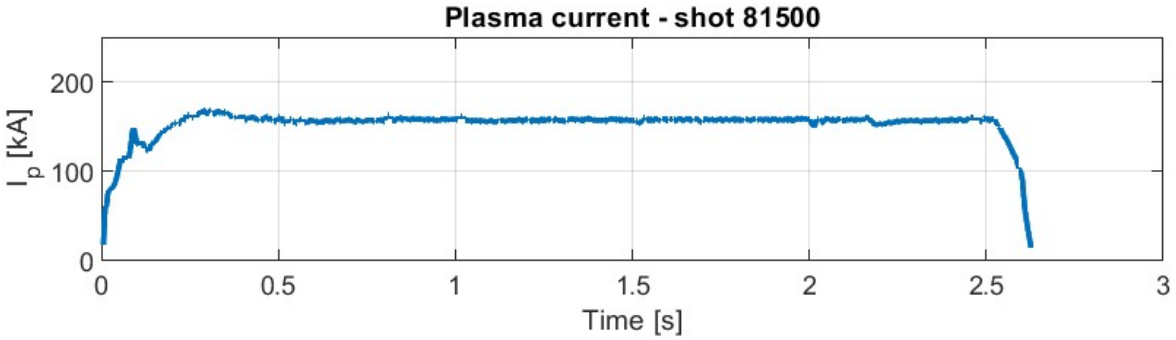

Figure 6.8: Plasma current measured during shot 81500.

The microwave injection was provided by three gyrotrons (G1, G10, G11), all operating in X2 mode. Each gyrotron injected a different level of power through distinct launchers and within different time intervals:

- G1: 650 kW through launcher L1, in the time interval [0.8, 2] s
- G11: 850 kW through launcher L4, in the time interval [0.8, 2] s
- G10: 850 kW through launcher L5, in the time interval [1, 2] s

While L1 and L4 injected in the same direction as the plasma current, L5 was oriented in the opposite direction, since it was proven that this configuration improved plasma stability. Table 6.2 lists the parameters for each gyrotron/launcher pair, including the poloidal (θ) and toroidal (ϕ) angles of the launchers, defined accordingly with the coordinate system illustrated in Figure 3.7a.

Table 6.2: ECRH parameters for shot 81500.

Gyrotron/launcher	Power [kW]	θ [°]	ϕ [°]	ECRH times [s]
G1/L1	650	17	-130	$0.8 \rightarrow 2$
G11/L4	850	17	-130	$0.8 \rightarrow 2$
G10/L5	850	46.6	8	$1 \rightarrow 2$

Figure 6.8 shows the plasma current measured during shot 81500, which remained almost constant at approximately 160 kA for the entire duration of the experiment.

Shot 85111

The first shot performed to test the validity of the Angle_opt optimization tool aimed at reproducing the scenario obtained in shot 81500, in order to collect more recent data. The ECRH parameters such as injection angles and injected power were therefore kept the same as in the original shot, with the only exception that launcher L5 began injecting at 0.8 s after the breakdown as the other two launchers, instead of at 1 s, due to an ECRH operator error. Additionally, the NBI-1 system was not used in any of the experiments due to unavailability. Both of these differences are not expected to have a significant impact on the results.

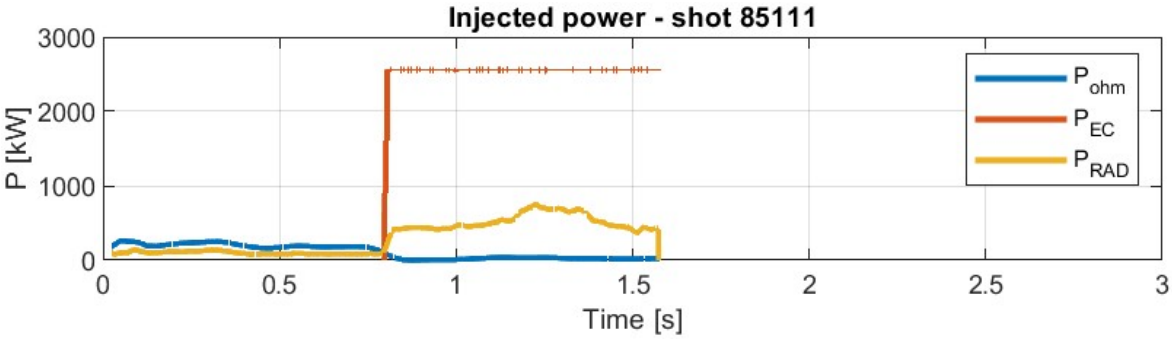

Figure 6.9: Power injected by the different systems during shot 85111.

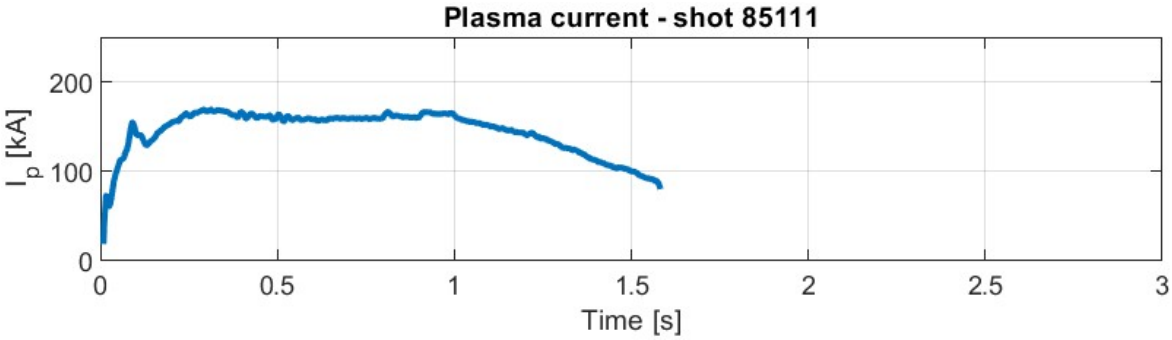

Figure 6.10: Plasma current measured during shot 85111.

Figure 6.9 shows the total power injected into the vessel by the different systems, while the measured plasma current is presented in Figure 6.10. At 1.58 s, the plasma faced a disruption as a result of a discharge in one of the gyrotrons waveguides. It can also be seen that the plasma current remained stable at 160 kA while ohmic power was injected, but began to decrease rapidly once the inductive drive ceased, indicating

that ECCD alone was insufficient to sustain a constant current for the entire duration of the shot.

For the moment, the fact that the measured current was significantly lower than in the original shot will be disregarded, leaving a possible explanation to Section 6.2.2. Meanwhile, shot 85111 will be considered as the reference scenario for comparison with other launcher configurations, in order to evaluate whether an improvement in the current driven by the ECCD system can be achieved by modifying the injection angles.

The optimization tool was therefore executed on shot 85111 to identify the injection angles that maximize the current driven into the plasma. Since at the beginning it was not clear why the current of shot 85111 was that low, Angle_opt was executed also on shot 81500, to check if the estimated optimal injection angle was the same in the two cases. The optimization considered the poloidal angle (θ) of launchers L1 and L4, while the toroidal angle (ϕ) was kept fixed at the value used in shot 81500. The injection direction of launcher L5 was left unchanged from the original shot, since its purpose was to enhance plasma stability rather than to contribute to current drive.

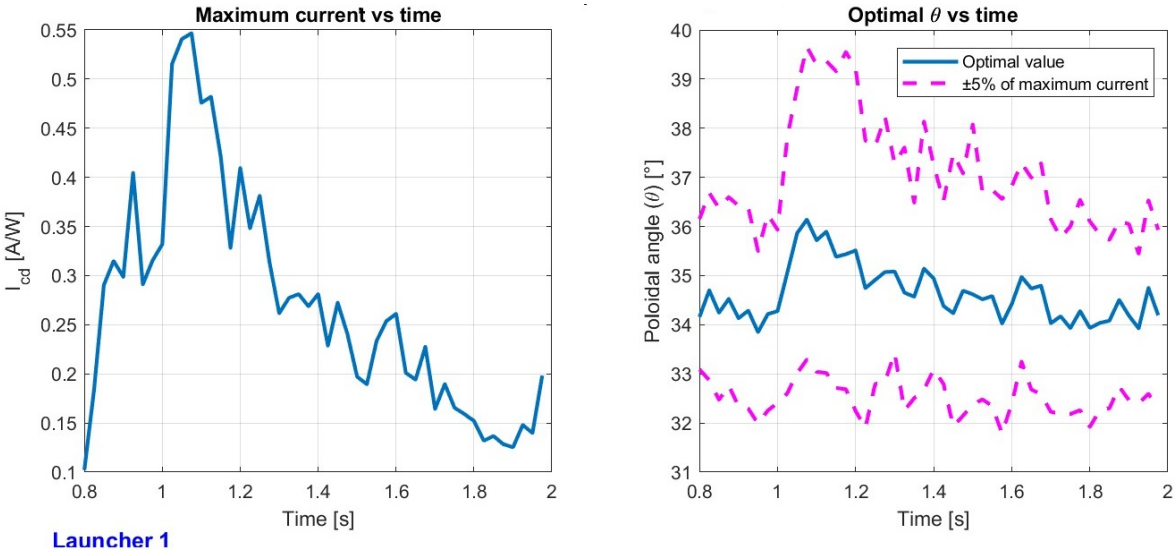

Figure 6.11: Results of the optimization of current drive for shot 81500.

The optimal poloidal angle for launcher L1 is shown in Figures 6.11 and 6.12, corresponding to shots 81500 and 85111, respectively. In both cases, the optimal poloidal angle remains nearly constant throughout the discharge, around 34°–35°. The peaks observed in the right-hand graph of Figure 6.12 at approximately 1.3 and 1.4 s are related to anomalous oscillations in the electron temperature measurements, as shown in Figure 6.13.

The results for launcher L4 are exactly the same as those for L1, as the two launchers inject from the same poloidal location (see Figure 3.4b) and share the same coordinate reference system.

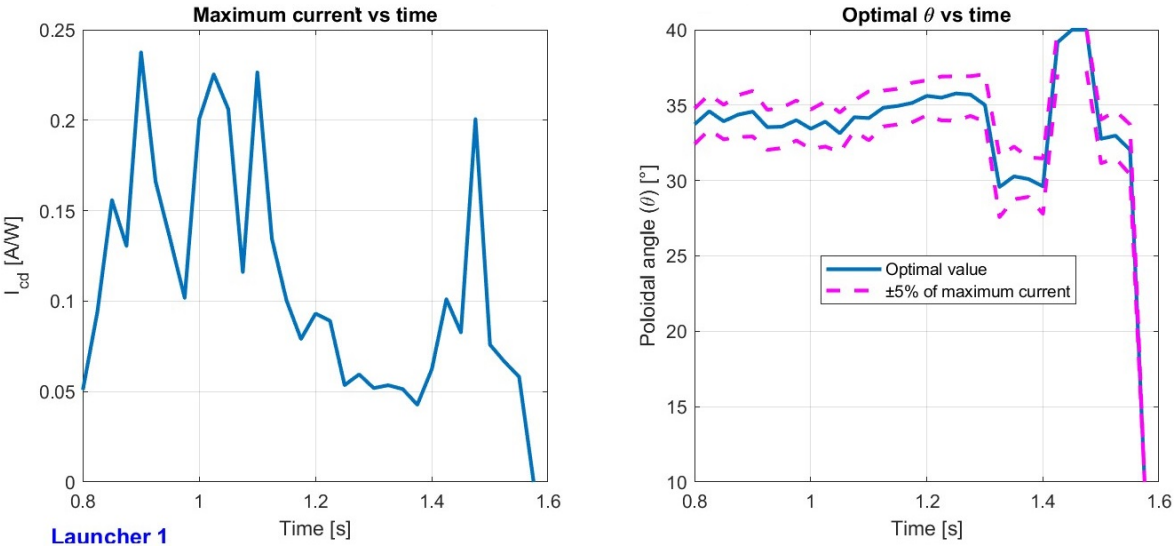

Figure 6.12: Results of the optimization of current drive for shot 85111.

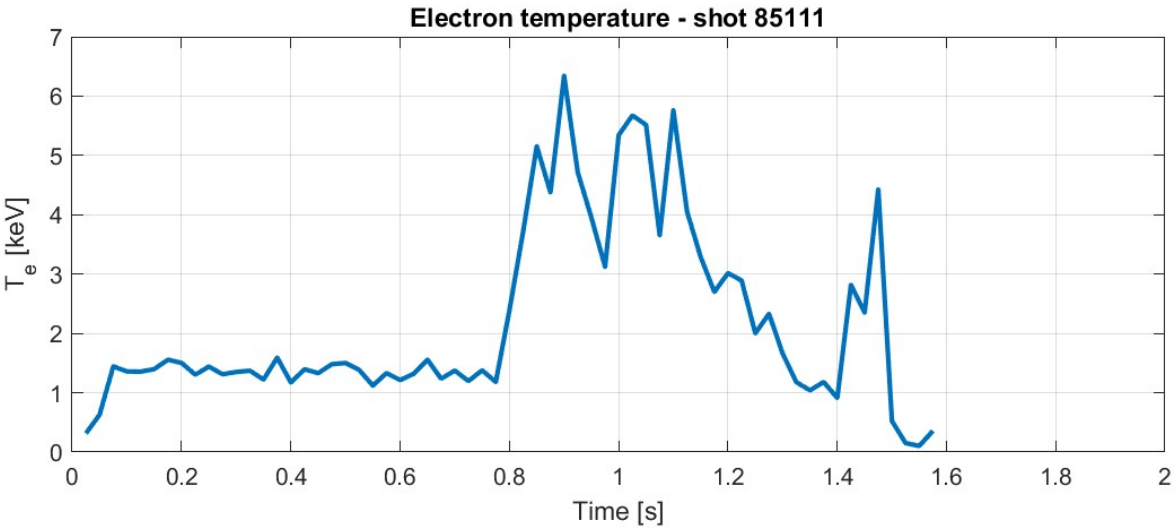

Figure 6.13: Electron temperature measured during shot 85111.

Shot 85114

Shot 85114 was performed maintaining the same parameters as the reference shot 85111, with the exception of the poloidal angle of launcher L1, which was increased to 25°. This value was adopted instead of the theoretical optimum of 35° to determine whether an improvement would be visible without significantly altering the configuration, as such a change could excessively modify the plasma equilibrium. Moreover, only the poloidal angle of launcher L1 was modified, while L5 was maintained in the same position as in shot 85111; this approach was chosen to isolate the impact of a single launcher optimization without introducing multiple variables.

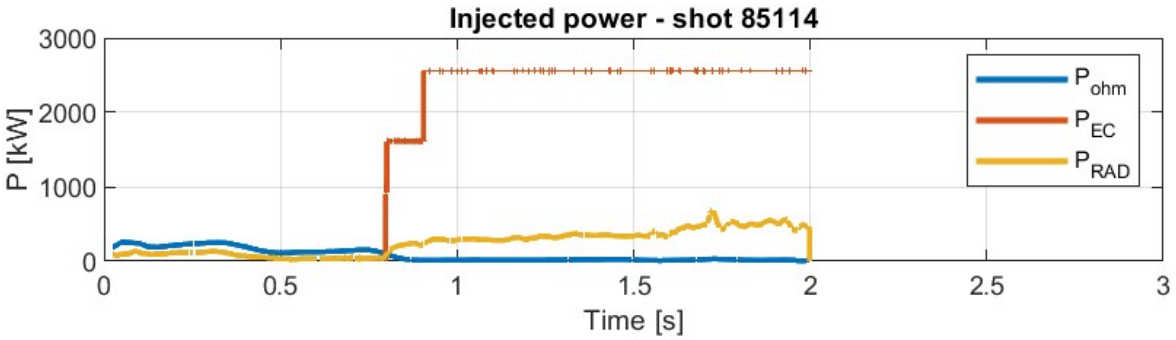

Figure 6.14: Power injected by the different systems during shot 85114.

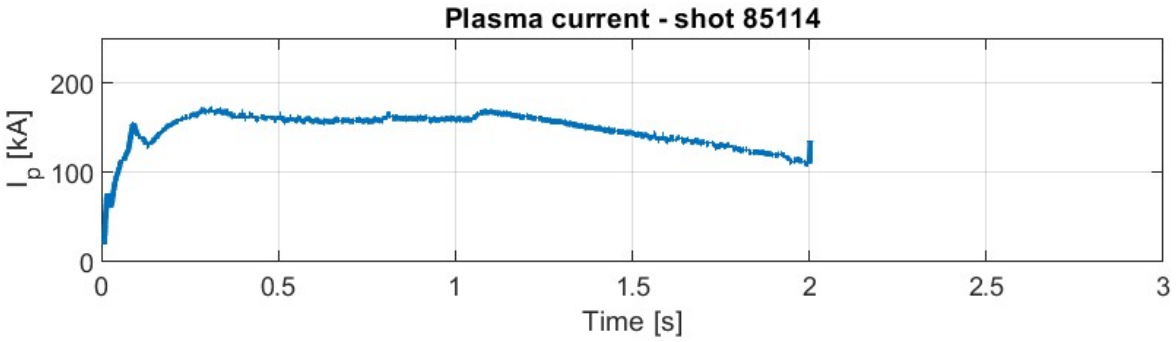

Figure 6.15: Plasma current measured during shot 85114.

An additional minor modification was introduced compared to shot 85111: the ohmic power was clamped at 0.9 s after the breakdown instead of 0.8 s, to investigate whether this could sustain the plasma current for a longer duration. Figure 6.14 shows the power injected from all systems, while the total current measured in the plasma during the shot is presented in Figure 6.15. It can be seen that, even with the new configuration, the current rapidly decreases after the ohmic power is turned off. However, a qualitative comparison with Figure 6.10 suggests a slight improvement with respect to the base configuration of shot 85111.

Shot 85115

The aim of this shot was to inject microwaves using the optimized angles computed by Angle_opt, in order to evaluate whether an improvement in plasma current could be achieved compared to the precedent experiments. Therefore, the poloidal angle of launcher L1 was increased to 34°, while all other parameters were kept the same as in shot 85114. Data regarding injected power and plasma current are presented in Figures 6.16 and 6.17. A slight improvement in the plasma current can be observed compared with shot 85114, although the current still decays rapidly after the ohmic power is clamped. Plasma confinement was lost after 1.76 s.

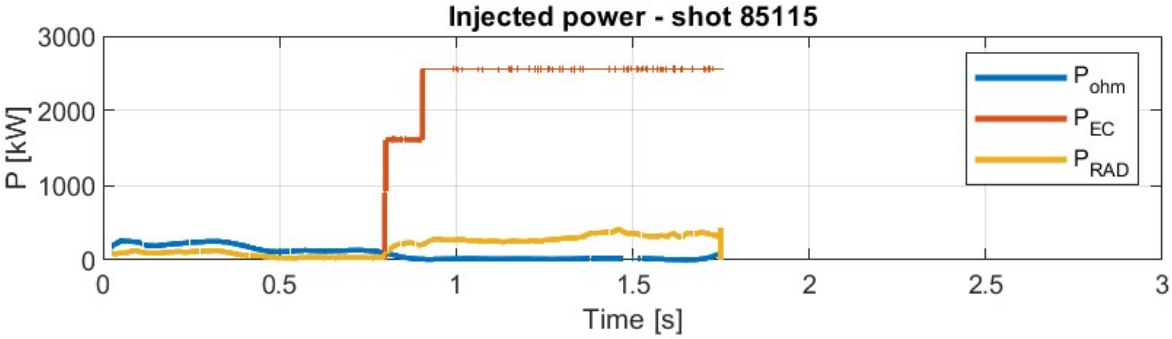

Figure 6.16: Power injected by the different systems during shot 85115.

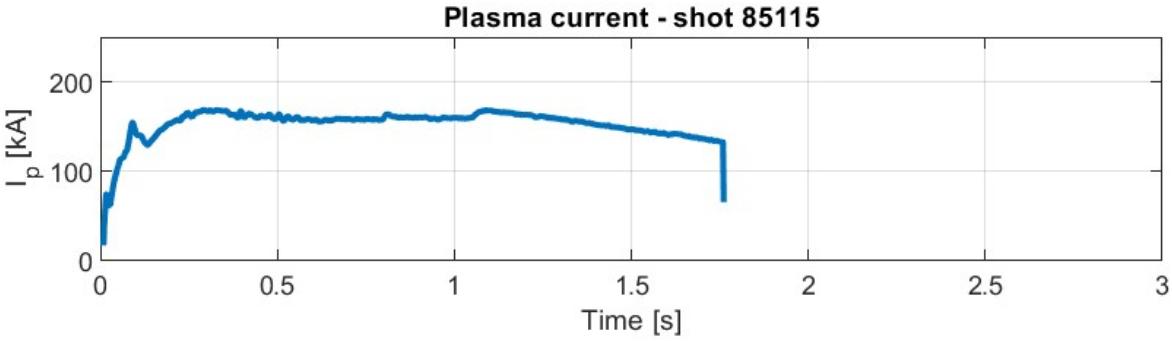

Figure 6.17: Plasma current measured during shot 85115.

Shot 85116

In the final experiment, the poloidal injection angle of launcher L1 was reduced to 25°, and this same angle was also adopted for launcher L4. The resulting measures are shown in Figures 6.18 and 6.19. A comparison with the previous shots clearly shows a significant improvement in the driven current, demonstrating that if the injection angle θ is increased for both launchers L1 and L4 instead of only L1, an important enhancement of the plasma current is obtained, even by adopting angles smaller than

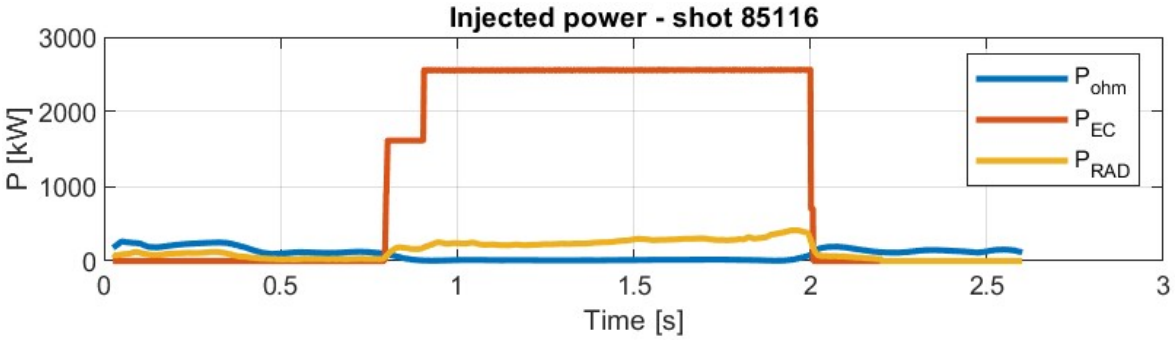

Figure 6.18: Power injected by the different systems during shot 85116.

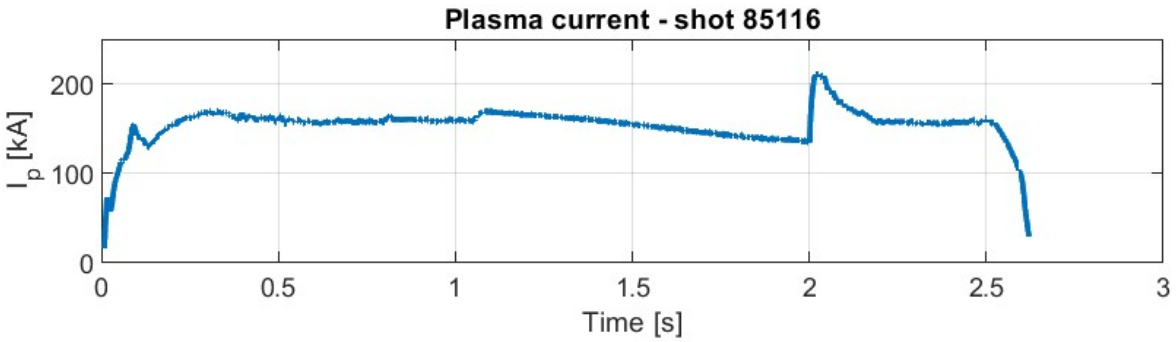

Figure 6.19: Plasma current measured during shot 85116.

the one calculated by Angle_opt. The peak in plasma current after 2 s, visible in Figure 6.19, is due to the ohmic current being turned on again. Therefore, the portion of the discharge relevant for the experiment is limited to the first two seconds.

A summary of the launcher angles adopted for each shot is presented in Table 6.3. The purpose of this section was to present the setup and results of the experiments conducted on TCV to test the Angle_opt optimization tool. A more detailed comparison and discussion of the experimental outcomes are presented in the following sections.

6.2.2 Comparison with the original shot

Section 6.2.1 highlighted a critical issue with the experimental shots: the current driven by EC waves was consistently lower than in shot 81500, causing the overall plasma current to decay after the ohmic heating was shut down. To address this problem, a comparison between shots 81500 and 85111 should be considered. Shot 81500 served as a reference for all experiments, while shot 85111 was designed to replicate the same plasma equilibrium. Despite this objective, plasma current measurements reveal substantial differences between the two scenarios.

The current profiles presented previously were obtained from TCV diagnostics, which provide reliable measurements of the total plasma current but cannot distin-

Table 6.3: Poloidal (θ) and toroidal (ϕ) angles adopted in the different shots for each launcher. The values that were modified with respect to the original scenario are highlighted in blue.

Shot number	Launcher L1	Launcher L4	Launcher L5
81500	$\theta = 17°$ $\phi = -130°$	$\theta = 17°$ $\phi = -130°$	$\theta = 46.6°$ $\phi = 8°$
85111	$\theta = 17°$ $\phi = -130°$	$\theta = 17°$ $\phi = -130°$	$\theta = 46.6°$ $\phi = 8°$
85114	$\theta = 25°$ $\phi = -130°$	$\theta = 17°$ $\phi = -130°$	$\theta = 46.6°$ $\phi = 8°$
85115	$\theta = 34°$ $\phi = -130°$	$\theta = 17°$ $\phi = -130°$	$\theta = 46.6°$ $\phi = 8°$
85116	$\theta = 25°$ $\phi = -130°$	$\theta = 25°$ $\phi = -130°$	$\theta = 46.6°$ $\phi = 8°$

guish between the EC-driven current and the inductively driven current. The isolation of the ECCD contribution can be achieved by performing TORAY simulations. These simulations can recreate the experimental plasma configuration and calculate the current driven by each gyrotron individually, at the cost of less precise results, due to the physical simplifications introduced with the computational model and the lack of a feedback loop in the simulation scripts, as discussed in Section 4.2.

To investigate the discrepancy between shots 81500 and 85111, the toray_automatic script was employed. The plasma equilibrium from each experiment served as input to the simulation, which then modeled the microwave injection using the exact parameters of the actual shots. This enabled the estimation of the total current driven by the three active gyrotrons in both shots, as illustrated in Figures 6.20 and 6.21.

Figure 6.20 shows that TORAY simulated a current for shot 81500 with a peak slightly above 160 kA – resulting in a small overestimation compared to the experiment – but immediately started to decrease, deviating significantly from the experimental measurements. This discrepancy can be explained by observing that in reality during shot 81500 the ohmic power was not completely disabled but rather modulated to maintain a constant current, as can be seen in Figure 6.7.

The corresponding analysis for shot 85111 is presented in Figure 6.21. Although the current follows a similar decay pattern to shot 81500, the initial value is substantially lower, with a peak of less than 80 kA compared to 160 kA in the reference scenario. Having such a low current would explain why the plasma current dropped rapidly once

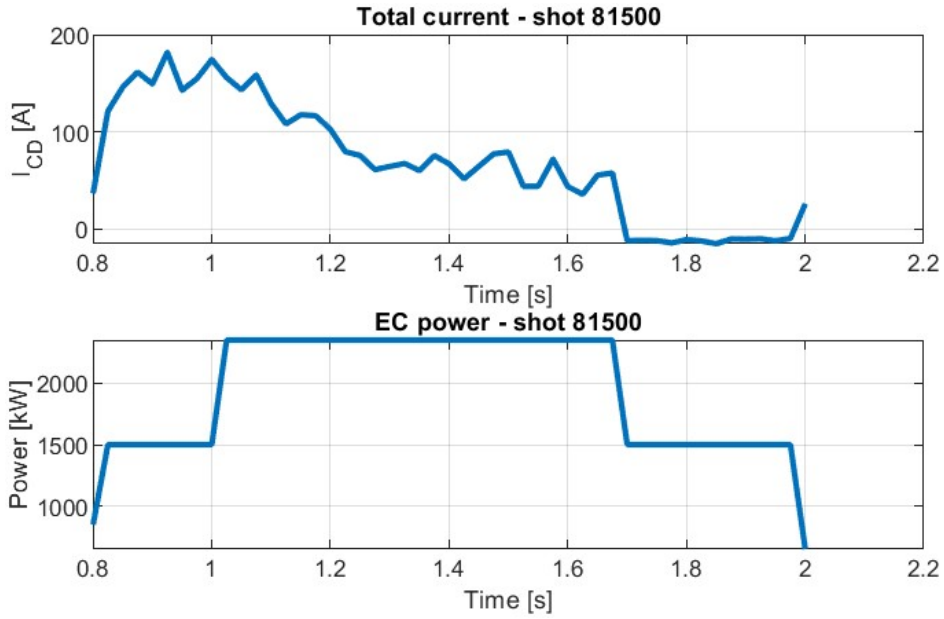

Figure 6.20: Plasma current driven by microwave injection overt time for shot 81500, simulated using TORAY.

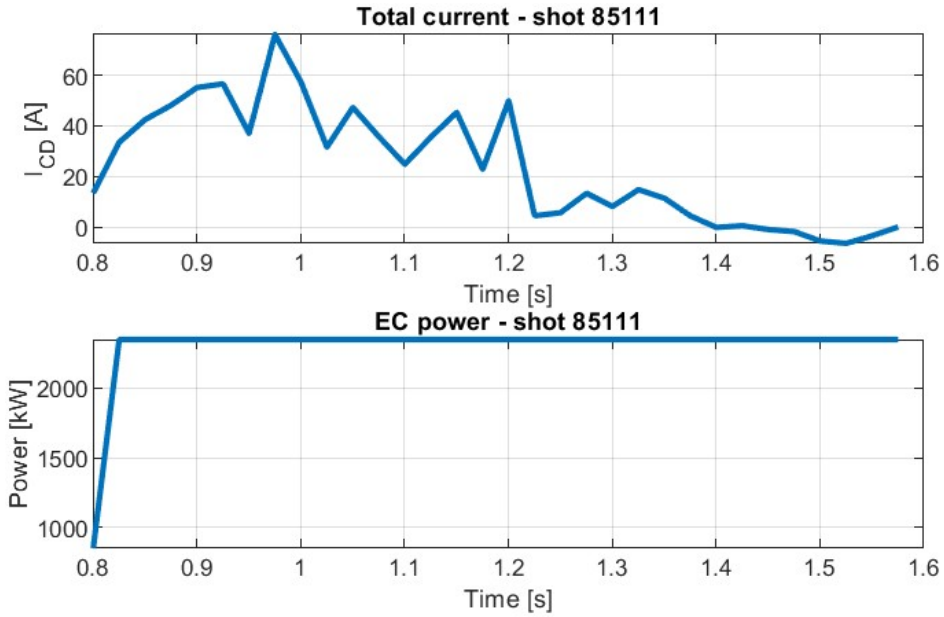

Figure 6.21: Plasma current driven by microwave injection over time for shot 85111, simulated using TORAY.

the ohmic heating was shut down in the experimental shots.

What remains to be explained is why the measured ECCD-driven current tends to decrease over time; the answer lies in the plasma density and temperature, since both parameters strongly influence current drive efficiency and EC wave absorption. The correlation between the current simulated by TORAY and the temperature and density measured during the experiments is presented in Figures 6.22 and 6.23 for shots 81500 and 85111, respectively.

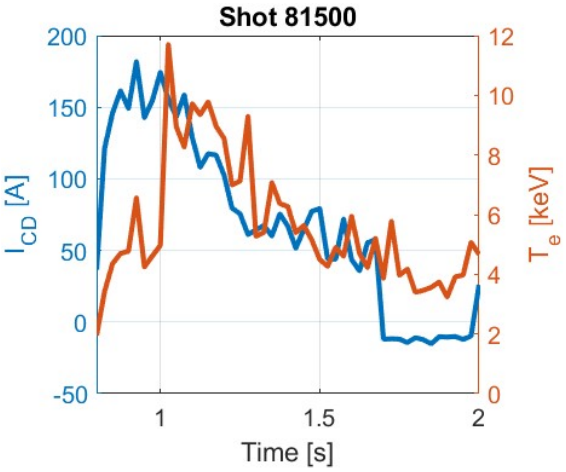

(a) Direct dependence between plasma current and temperature, over time.

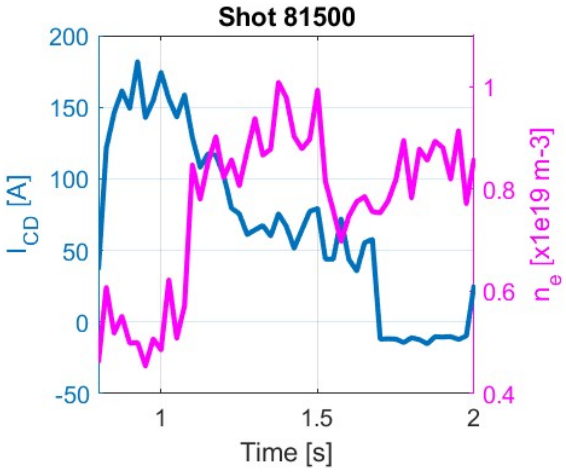

(b) Inverse dependence between plasma current and density, over time.

Figure 6.22: Comparison between plasma current and temperature and density trends, for shot 81500. The current was simulated via TORAY, while temperature and density were measured during the experiment in the central region of the plasma.

A clarification regarding the plasma measurements is necessary. Plasma temperature and density are measured over time by multiple sensors distributed across the tokamak's minor radius; in the aforementioned figures, only the sensor closest to the plasma center was considered. This choice was made because the plasma core is the region of primary interest, as current drive occurs predominantly in this area.

The figures clearly demonstrate a strong positive correlation between plasma temperature and driven current, while an inverse correlation exists between plasma density and current. This relationship explains the temporal decay of the current in both simulated scenarios. Additionally, it can be observed that the plasma density measured in shot 85111 is higher than the density measured for shot 81500. For a given injected power, a higher plasma density results in smaller temperature increases, as the energy must be distributed among more particles. Therefore, the elevated plasma density in shot 85111 can explain the lower plasma temperature compared to shot 81500. Consequently, if during the shots the vacuum conditions inside the vessel were compromised for any reason, this would increase plasma density and consequently reduce

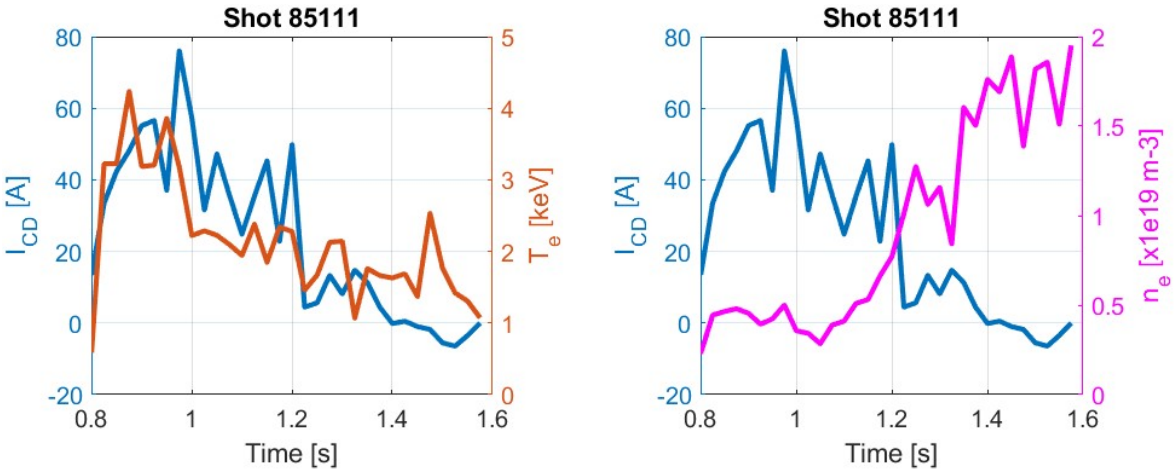

(a) Direct dependence between plasma current and temperature, over time.

(b) Inverse dependence between plasma current and density, over time.

Figure 6.23: Comparison between plasma current and temperature and density trends, for shot 85111.

temperature. Given the established relationship between plasma properties and the driven current, the unexpectedly low current values in shot 85111 can be attributed to anomalously high plasma density.

To support the reasoning just presented, the first step was to quantify the differences in plasma temperature and density between the two shots. The electron temperature and density of shots 81500 and 85111 were compared by averaging these quantities over time. The resulting time-averaged profiles are shown in Figures 6.24 and 6.25 for both shots. Subsequently, a spatial average over the radial profiles was performed, considering only the region of the plasma from the axis (a=0, where a is the dimensionless minor radius of the tokamak) up to a=0.8. This is justified by the fact that the driven current is predominantly confined to the core region, whereas the outer plasma contributes negligibly and can be excluded. In this way, two values indicative of the average plasma temperature and density were obtained for each shot. These quantities are denoted as $T^{shot}_{e\_avg}$ and $n^{shot}_{e\_avg}$.

By taking the ratios of the corresponding values between the two shots, two coefficients were calculated to quantify the discrepancy in plasma conditions between shots 81500 and 85111. These coefficients are indicative not only of how different the scenarios are, but can also help assess whether the observed differences in the plasma current could be attributed to these changes in plasma parameters. This analysis was made possible thanks to a feature of toray_automatic, which allows for rescaling the plasma temperature and density profiles before simulating the microwave injection. The idea was to scale the profiles measured for shot 85111, in order to reproduce a plasma scenario closer to that of shot 81500, so that the simulation results could be

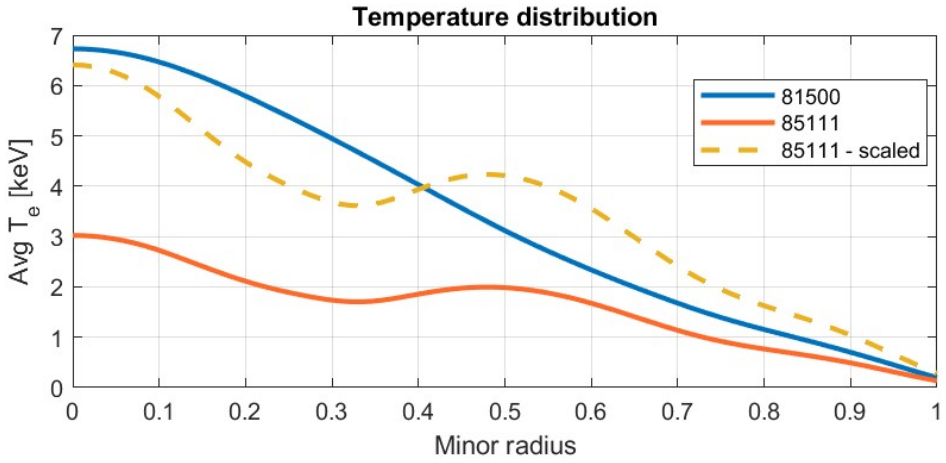

Figure 6.24: Comparison of the time-averaged temperature distribution of shots 81500 and 85111. The dashed yellow curve represents the profile of shot 85111 scaled to match the plasma conditions of shot 81500.

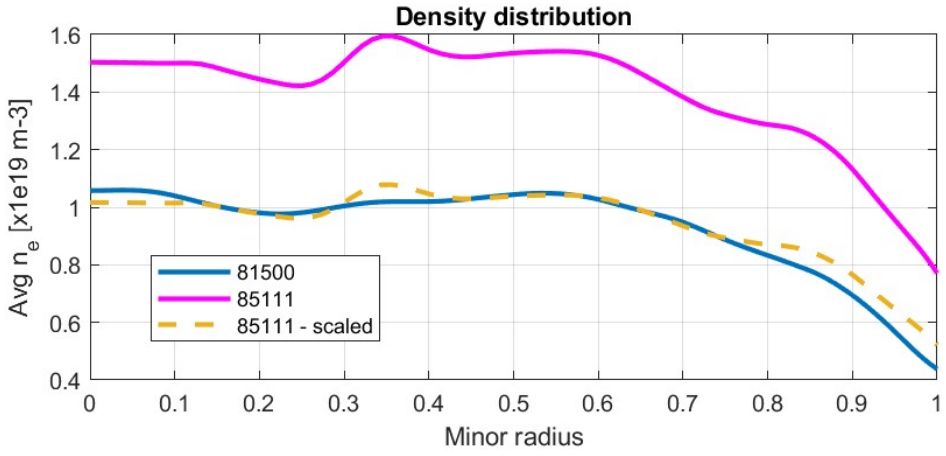

Figure 6.25: Comparison of the time-averaged density distribution of shots 81500 and 85111. The dashed yellow curve represents the profile of shot 85111 scaled to match the plasma conditions of shot 81500.

directly compared, now sharing not only the same launcher parameters but also similar plasma conditions. The dashed yellow curves in Figures 6.24 and 6.25 represent the scaled profiles of shot 85111, adjusted to match those of shot 81500.

The scaling factors used were as follows:

$$\frac{T_{e\_avg}^{81500}}{T_{e\_avg}^{85111}} = 2.12 \quad \text{and} \quad \frac{n_{e\_avg}^{81500}}{n_{e\_avg}^{85111}} = 0.68 \tag{6.1}$$

A new simulation was then run for shot 85111 using toray_automatic, now with the two scaling factors provided as additional input. The resulting driven current is shown in Figure 6.26, where it is compared with the one already obtained from the simulation of shot 81500. In Figure 6.26, it is qualitatively clear that, with scaled

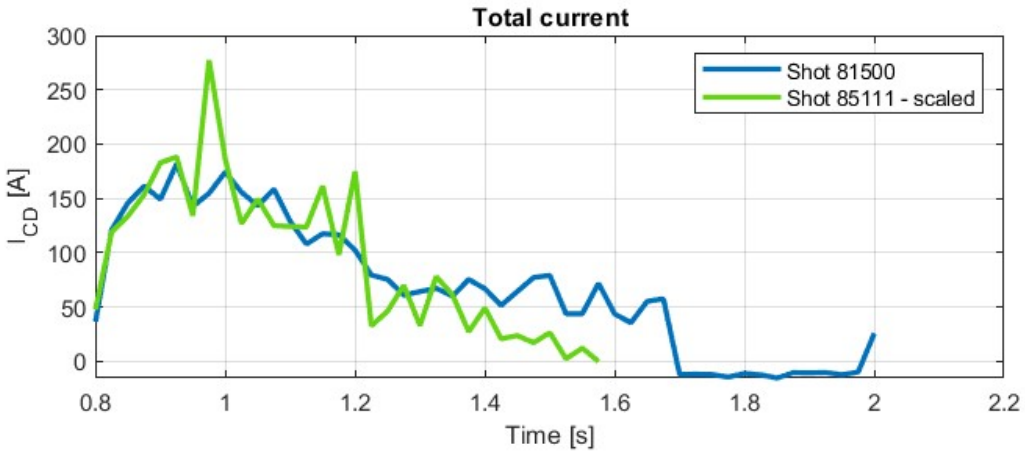

Figure 6.26: Plasma current simulated via TORAY for shots 81500 and 85111. The curve for shot 85111 was scaled using the scaling factors given by Eqn. 6.1, in order to match the same plasma parameters of shot 81500.

plasma parameters, the current predicted by TORAY is of the same order of magnitude as the one predicted for 81500. This confirms that the discrepancy between the original and the new shots is mainly due to differences in plasma temperature and density, likely caused by different initial vacuum conditions in the vessel.

In summary, as seen in Section 6.2.1, in all the experiments carried out to test the Angle_opt optimization tool, the current decayed rapidly, in contrast to what was observed in the original shot 81500. This section aimed to justify this behavior by hypothesizing that the initial gas condition in the vessel resulted in a density higher than expected. This affected the plasma temperature and, consequently, the plasma current, significantly reducing the maximum value achievable with the ECCD system. This hypothesis was supported by additional simulations with scaled temperature and density, a necessary measure to reproduce a plasma equilibrium similar to the one observed in shot 81500.

Of course, this method presented here had only a qualitative purpose, aiming to provide an explanation of what was measured. Several simplifications and errors were introduced during this process, firstly, the arbitrary choice of the extent of the plasma area to be excluded from the scaling coefficient calculation, which was not based on a strict physical criterion, but also the limitations of the simulation itself, which were already highlighted. These constraints made it impossible to achieve a reliable and precise comparison between the original and the new shots. A more meaningful comparison could only be obtained by repeating the experiments, ensuring plasma conditions comparable to the original scenario, something that was not feasible due to time constraints.

6.2.3 Comparison between the new shots

The differences in plasma parameters between the new experiments and shot 81500 made any direct comparison with the original shot meaningless, unless plasma temperature and density of the shot in question were rescaled to match the same plasma equilibrium observed for shot 81500. However, since all the new shots were affected by this issue in the same way, a comparison between them remained valid. This allowed to verify whether optimized injection angles led to improvements in current drive compared to unoptimized ones.

Figure 6.27 compares the plasma current measured for all the shots performed. A significant improvement can be seen when a poloidal angle of 25° is used for launcher L1, as in shot 85114, compared to shot 85111, where the injection angle was 17°. The optimal angle computed by Angle_opt is 34°, and it was adopted in shot 85115. A slight improvement in the plasma current is observed with respect to shot 85114, though not so relevant. Finally, in shot 85116 a poloidal angle of 25° was apply not only to launcher L1 but also to L4, leading to a marked improvement in plasma current compared with all the other scenarios.

An additional aspect should be considered: by varying the poloidal injection angle, not only the value of the current changes, but also its radial position does. To highlight this fact, two more simulations were performed based on shot 85111, using different angles θ for launcher L1. Figure 6.28[1] shows the current distribution along the tokamak minor radius, driven by launcher L1 in the two cases. The two curves were obtained by simulating EC injection using the GUIprofs interface, adopting a poloidal angle of 17° in one case and 34° in the other. From the comparison, it is clear that increasing the injection angle shifts the driven current closer to the plasma center.

[1] Here the sign of the current is taken as negative, according to the GUIprofs reference system. In the following, all comparisons between the two curves consider the absolute value of the current, disregarding the sign.

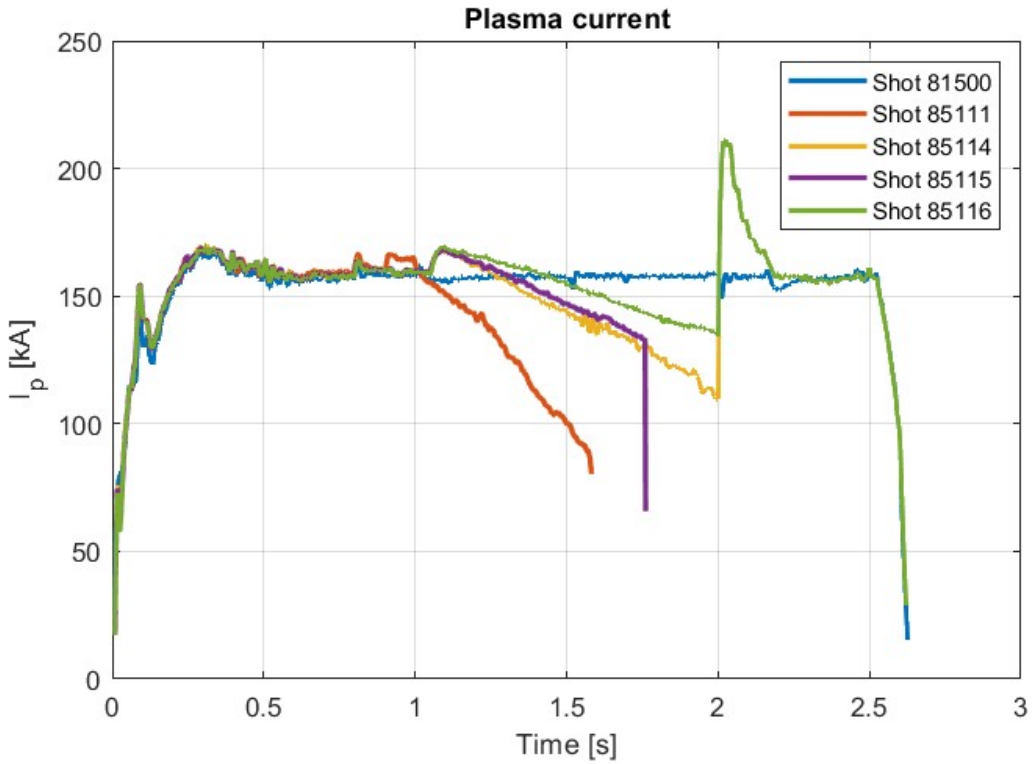

Figure 6.27: Plasma current measured for all the shots performed in the context of the ECCD optimization scenario. The optimal angles estimated by Angle_opt seem to enhance the EC current drive.

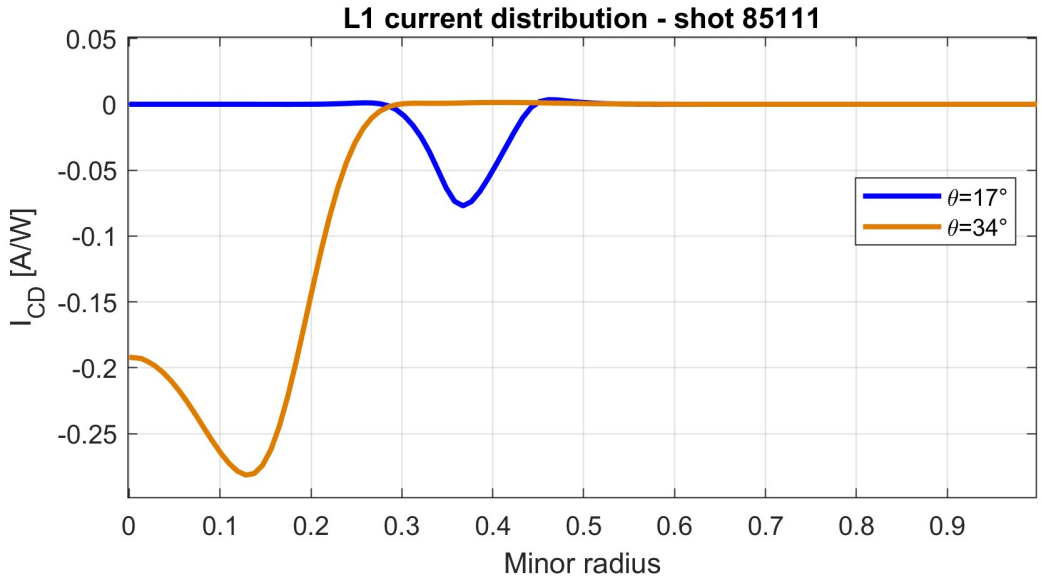

Figure 6.28: Current distributions driven by launcher L1 for shot 85111, simulated using GUIprofs. The two curves are plotted representing the injection with θ at 17° and 34°. Increasing θ, the plasma current is shifted toward the center of the plasma.

The observed radial shift of the current may alter the plasma equilibrium, potentially triggering plasma MHD instabilities or transport phenomena, which could negatively affect the overall EC current drive. In the same figure, it can be seen that TORAY predicts a much higher plasma current for the scenario adopting θ=17°, compared to that with the injection at 34°; the reason why in the experiments the improvement is much lower could also be explained by considering the possible presence of MHD instabilities when the current is driven closer to the plasma center – an effect disregarded in TORAY simulation.

Chapter 7

Conclusions

The work developed in this thesis had the purpose of developing a numerical code capable of estimating the optimal EC wave injection angle maximizing either the fraction of absorbed power or the driven current, specifically for TCV. The final goal was to provide the EC operator in the TCV control room with a tool capable of orienting the choice of launcher injection angles for a specific plasma scenario before performing an experiment. This would substitute the approach currently used based mainly on previous experiences and on a try-and-error approach.

The Angle_opt tool, which was developed in MATLAB following this purpose, exploits other scripts to simulate the injection of EC waves in a given plasma scenario, at multiple times. This allows to define the optimal injection angle independently for different launchers, optimizing a certain parameter such as power absorption or current drive. In particular, Angle_opt could be particularly useful in the case of plasmas with parameters changing over time. In these scenarios the optimal injection angles may vary sensibly during the discharge, following the changing plasma equilibrium; a time-dependent optimization could therefore be particularly beneficial, allowing to exploit the capability of the launcher's mirrors to vary their orientation during the operation.

After developing the Angle_opt tool with the objectives mentioned above, experiments were carried out to test the functionality of the tool, and access whether it needed further improvements. Two different campaigns were carried out, one with the aim of maximizing the power deposition inside the plasma and the other to optimize a non-inductive current drive.

The optimization of power deposition was tested in a plasma scenario in which the plasma moved downward during the discharge. This choice was made in order to test a time-dependent optimization. Three shots were taken to check the performance of Angle_opt: a reference shot, necessary for the comparisons between experiments, a second shot to observe the dependence of the power from the injection angle, and a third one adopting the optimal poloidal injection angle θ provided by Angle_opt. In

particular, in the last shot the optimal injection angle changed over time, exploiting in this way the time-dependent optimization provided by the tool. The absorption efficiency of the reference shot was already high, but by adopting the optimized angles an improvement in the power deposition could still be observed, especially at the at the end of the plasma discharge, when the plasma moved closer to the bottom of the vessel.

The current drive optimization was tested in a scenario with no ohmic heating, i.e. the current was driven only by the ECCD and NBI systems. One shot was chosen as a reference, and many other plasma discharges were carried out in order to try to enhance the plasma current with respect to the reference scenario. Due to an anomaly in the plasma density, all the experiments performed showed a value of current lower than expected, making any comparison with the original shot impossible. Nevertheless, since this issue was common for all the newly performed shots, a comparison between them was still possible: an improvement in the current was observed when EC waves were injected closer to the center of the plasma, as predicted by Angle_prof. However, this shift of the current toward the plasma center, consequent to the angle optimization, may have given origins to plasma instabilities, reducing the current improvement with respect to the expected one.

The two experimental campaigns presented in this work proved that Angle_opt could improve the efficiency with which the ECRH & ECCD system is used on TCV. The experiments performed with the aim of maximizing power deposition showed that the developed tool could be particularly useful in scenarios where the plasma parameters change over time, sensibly improving the power absorption compared to the case adopting constant injection angles. Angle_opt proved useful also in the maximization of current drive, but due to the complexity of the experiment and some unexpected issues they were less evident. This suggests that for complex plasma scenarios the tool may be less precise, and further adjustments on the results provided by the script should be introduced in order to account for more complicate physical aspects.

In both cases, the angles estimated by Angle_opt provided an improvement in the parameter to be optimized, making it possible to conclude that the tool could be useful in providing to the ECH operator a first indication on the choice of the injection parameters. Lacking a feedback loop and disregarding more complex plasma phenomena, Angle_opt can only give a qualitative orientation, which can be subsequently adjusted on the basis of the experience or experimental data.

As further development of this thesis, additional experiments could be carried out in the contest of the current optimization, in order to assess whether the encountered discrepancy between the reference shot and the experiments is effectively explainable with an anomalously high plasma density. Moreover, additional diagnostic systems should be employed in order to better define the type of instabilities rising with cur-

rents in proximity to the plasma center and quantify their entity. The Angle_opt optimization tool should also be tested for other different plasma scenarios to assess its reliability under different conditions.

Further improvements of the optimization tool could include the addition of an option to maximize the power deposition at a certain plasma magnetic surface, which was already roughly implemented in the code but was not tested through experiments, as well as the development of a graphical interface to be included directly on the ECH operator interface.

References

[1] E. Margaret Burbidge, G. R. Burbidge, William A. Fowler, and F. Hoyle. Synthesis of the elements in stars. *Rev. Mod. Phys.*, 29:547–650, Oct 1957. doi: 10.1103/RevModPhys.29.547. URL https://link.aps.org/doi/10.1103/RevModPhys.29.547.

[2] IEA. Global Energy Review 2025. Technical report, Paris, 2025. URL https://www.iea.org/reports/global-energy-review-2025.

[3] IEA. Global energy system. URL https://www.iea.org/world.

[4] Florinda Martins, Carlos Felgueiras, Miroslava Smitkova, and Nídia Caetano. Analysis of fossil fuel energy consumption and environmental impacts in european countries. *Energies*, 12(6), 2019. ISSN 1996-1073. doi: 10.3390/en12060964. URL https://www.mdpi.com/1996-1073/12/6/964.

[5] A. Kirk and. Nuclear fusion: bringing a star down to earth. *Contemporary Physics*, 57(1):1–18, 2016. doi: 10.1080/00107514.2015.1037076. URL https://doi.org/10.1080/00107514.2015.1037076.

[6] Hiroshi Yamada. *Fusion Energy*, pages 3139–3171. Springer International Publishing, Cham, 2017. ISBN 978-3-319-14409-2. doi: 10.1007/978-3-319-14409-2_31. URL https://doi.org/10.1007/978-3-319-14409-2_31.

[7] John Wesson. *Tokamaks; 4th ed.* International series of monographs on physics. Oxford Univ. Press, Oxford, 2011.

[8] EUROfusion. Eurofusion official website, 2025. URL https://www.eurofusion.org/.

[9] Dale Meade. 50 years of fusion research. *Nuclear Fusion*, 50(1):014004, dec 2009. doi: 10.1088/0029-5515/50/1/014004. URL https://dx.doi.org/10.1088/0029-5515/50/1/014004.

[10] Pietro Vincenzi. Plasma heating and current drive (icrh, ecrh, nbi). Slide presentation, 2023. Lecture slides from the course "Thermonuclear Fusion", Master's Degree in Electrical Energy Engineering, University of Padua (A.Y. 2022/23).

[11] Nathaniel J. Fisch. Theory of current drive in plasmas. *Rev. Mod. Phys.*, 59: 175–234, Jan 1987. doi: 10.1103/RevModPhys.59.175. URL https://link.aps.org/doi/10.1103/RevModPhys.59.175.

[12] Francis F. Chen. *Plasma Applications*. Springer International Publishing, Cham, 2016. ISBN 978-3-319-22309-4. doi: 10.1007/978-3-319-22309-4_10. URL https://doi.org/10.1007/978-3-319-22309-4_10.

[13] *Fundamentals of Magnetic Fusion Technology*. Non-serial Publications. INTERNATIONAL ATOMIC ENERGY AGENCY, Vienna, 2023. ISBN 978-92-0-110721-3. URL https://www.iaea.org/publications/14898/fundamentals-of-magnetic-fusion-technology.

[14] TCV auxiliary heating, . URL https://www.epfl.ch/research/domains/swiss-plasma-center/research/tcv/research_tcv_heating/.

[15] Naima Ghoutia and Sabri Sabri. Production of high power by using gyrotron device for electron cyclotron resonance heating in tokamak reactor. *Energy Procedia*, 18:944–953, 2012. ISSN 1876-6102. doi: https://doi.org/10.1016/j.egypro.2012.05.109. URL https://www.sciencedirect.com/science/article/pii/S187661021200879X. Terragreen 2012: Clean Energy Solutions for Sustainable Environment (CESSE).

[16] Matsusada Precision. Gyrotron applications, n.d. URL https://www.matsusada.com/application/ps/gyrotron/. Accessed: July 2025.

[17] Katsumichi HOSHINO and. Electron cyclotron heating (ech) of tokamak plasmas. *Journal of Nuclear Science and Technology*, 27(5):391–405, 1990. doi: 10.1080/18811248.1990.9731201. URL https://doi.org/10.1080/18811248.1990.9731201.

[18] Enrico Zilli. *Elementi di Fisica del Plasma*.

[19] Egbert Westerhof. Electron cyclotron waves. *Fusion Science and Technology*, 61: 304–311, 02 2012. doi: 10.13182/FST12-A13517.

[20] Heinrich Peter Laqua. Electron bernstein wave heating and diagnostic. *Plasma Physics and Controlled Fusion*, 49(4):R1, mar 2007. doi: 10.1088/0741-3335/49/4/R01. URL https://dx.doi.org/10.1088/0741-3335/49/4/R01.

[21] TCV Tokamak, . URL https://www.epfl.ch/research/domains/swiss-plasma-center/research/tcv/research_tcv_tokamak/.

[22] TCV general information, . URL https://spcwiki.epfl.ch/wiki/TCV_general_information.

[23] Emmanuel Barraud. Warming up! 30 years of fusion research at EPFL | EPFL | Les dossiers de l'actu, September 2023. URL https://longread.epfl.ch/en/dossier/warming-up-30-years-of-fusion-research-at-epfl/.

[24] TCV ECH system, . URL https://spcwiki.epfl.ch/wiki/TCV_ECH_system.

[25] T.P. Goodman and the TCV team. Experience in integrated control of the multi-megawatt electron cyclotron heating system on the tcv tokamak: the first decade. *Nuclear Fusion*, 48(5):054011, apr 2008. doi: 10.1088/0029-5515/48/5/054011. URL https://dx.doi.org/10.1088/0029-5515/48/5/054011.

[26] Alexander N. Karpushov, Basil P. Duval, René Chavan, Emiliano Fable, Jean-Michel Mayor, Olivier Sauter, and Henri Weisen. A scoping study of the application of neutral beam heating on the tcv tokamak. *Fusion Engineering and Design*, 86(6):868–871, 2011. ISSN 0920-3796. doi: https://doi.org/10.1016/j.fusengdes.2011.02.077. Proceedings of the 26th Symposium of Fusion Technology (SOFT-26).

[27] Alexander N. Karpushov, Filippo Bagnato, Marcelo Baquero-Ruiz, Stefano Coda, Claudia Colandrea, Frédéric Dolizy, Jérémie Dubray, Basil P. Duval, Damien Fasel, Ambrogio Fasoli, Rémy Jacquier, Pierre Lavanchy, Blaise Marlétaz, Yves Martin, Lorenzo Martinelli, Dmytry Mykytchuk, Marta M. Pedrini, Jesús Poley, Holger Reimerdes, Umar Sheikh, Ugo Siravo, Matthieu Toussaint, and Matteo Vallar. Upgrade of the neutral beam heating system on the tcv tokamak – second high energy neutral beam. *Fusion Engineering and Design*, 187:113384, 2023. ISSN 0920-3796. doi: https://doi.org/10.1016/j.fusengdes.2022.113384.

[28] TCV control room, . URL https://spcwiki.epfl.ch/wiki/TCV_control_room.

[29] J. E. Kinsey and M. Choi. The TORAY Electron Cyclotron Heating and Current Drive Code. *General Atomics, La Jolla, CA 92186*, April 2003.

List of Figures

List of Tables

List of Abbreviations

DEMO Demonstration Fusion Power Reactor

DMPX Duplex Multiwire Proportional X-ray Counter

DNBI Diagnostic Neutral Beam Injector

EBW Electron Bernstein Wave

EC Electron Cyclotron

ECCD Electron Cyclotron Current Drive

ECR Electron Cyclotron Resonance

ECRH Electron Cyclotron Resonance Heating

GUI Graphical User Interface

HFS High-Field Side

ICRH Ion Cyclotron Resonance Heating

ITER International Thermonuclear Experimental Reactor

LFS Low-Field Side

LHRH Lower Hybrid Resonance Heating

MHD Magneto Hydro Dynamic

MOU Matching Optics Unit

NBI Neutral Beam Injection/Injector

OH Ohmic Heating

RF Radio-Frequency

SPC Swiss Plasma Center

TCV Tokamak à Configuration Variable

TE Transverse Electric